11-2021

Energy Harvesting for Self-Powered Sensors for Smart Transportation Infrastructures

Anil K. Agrawal

Mohsen Amjadian
The University of Texas Rio Grande Valley, mohsen.amjadian@utrgv.edu

Hani Nassif

C2SMART
CONNECTED CITIES WITH SMART TRANSPORTATION
A USDOT University Transportation Center

New York University
Rutgers University
University of Washington
The University of Texas at El Paso
City College of New York

Energy Harvesting for Self-Powered Sensors for Smart Transportation Infrastructures

November 2021

Energy Harvesting for Self-Powered Sensors for Smart Transportation Infrastructures

Anil K. Agrawal
The City College of New York
0000-0001-6660-2299

Mohsen Amjadian
The University of Texas Rio Grande Valley
0000-0002-6786-8707

Hani Nassif
Rutgers University
0000-0002-3441-3589

C2SMART Center is a USDOT Tier 1 University Transportation Center taking on some of today's most pressing urban mobility challenges. Some of the areas C2SMART focuses on include:

Urban Mobility and Connected Citizens

Urban Analytics for Smart Cities

Resilient, Smart, & Secure Infrastructure

Disruptive Technologies and their impacts on transportation systems. Our aim is to develop innovative solutions to accelerate technology transfer from the research phase to the real world.

Unconventional Big Data Applications from field tests and non-traditional sensing technologies for decision-makers to address a wide range of urban mobility problems with the best information available.

Impactful Engagement overcoming institutional barriers to innovation to hear and meet the needs of city and state stakeholders, including government agencies, policy makers, the private sector, non-profit organizations, and entrepreneurs.

Forward-thinking Training and Development dedicated to training the workforce of tomorrow to deal with new mobility problems in ways that are not covered in existing transportation curricula.

Led by New York University's Tandon School of Engineering, **C2SMART** is a consortium of leading research universities, including Rutgers University, University of Washington, the University of Texas at El Paso, and The City College of NY.

Visit c2smart.engineering.nyu.edu to learn more

C2SMART
CONNECTED CITIES WITH SMART TRANSPORTATION

Disclaimer

The contents of this report reflect the views of the authors, who are responsible for the facts and the accuracy of the information presented herein. This document is disseminated in the interest of information exchange. The report is funded, partially or entirely, by a grant from the U.S. Department of Transportation's University Transportation Centers Program. However, the U.S. Government assumes no liability for the contents or use thereof.

Executive Summary

While there has been intense focus on ubiquitous sensing of transportation infrastructures, powering sensors and other peripherals by drawing wires from existing utility lines becomes cost-prohibitive and frequently complex operation. These sensors can be powered by alternative sources of power much more efficiently and at significantly cheaper costs. Harvesting energy from ambient vibration sources, including traffic-induced vibration of transportation infrastructures, is one of the most attractive options for powering ubiquitous sensors on transportation infrastructures. The highway statistics shows that the average daily vehicles miles travelled in the US is more than 5000 million, representing a massive source of kinetic energy that lies unused in the national transportation network. A large portion of this unused kinetic energy is generated by the daily traffic load on highway bridges and other transportation infrastructures in the form of low-frequency vibration. This kinetic energy can be effectively harvested to power sensors and monitoring peripherals. The proposed concept of the self-powered sensors relies on the use of existing sensors that could be powered by energy harvesters and could be installed at any part of a transportation infrastructure without elaborate wiring.

In this research project, an Electromagnetic Energy Harvesting System (EMEHS) is developed for harvesting the kinetic energy of ambient and traffic-induced vibrations and carry out a detailed feasibility study and impacts of such system for application on transportation infrastructures. The proposed EMEHS utilizes the innovative concept of creating array of large number of small permanent magnets through certain optimization criteria to achieve strong and focused magnetic field in a particular orientation. When these magnets are attached to a flexible sub-system and placed close to the copper coil, ambient and traffic-induced vibration of the sub-system induces eddy current in copper the coil which can be used to power sensors. The mass and stiffness of the sub-system are adjusted such that a low-frequency vibration due to the traffic load can effectively induce the vibration of the sub-system, and thereby increasing the output voltage. This vibration is further amplified by tuning the frequency of the sub-system to resonance condition.

The key innovation of the proposed research, as compared to other energy harvesters, is the optimization of array of permanent magnets for achieving a high electric power by developing an accurate analytical model for the magnetic interaction between the permanent magnets and the copper coil in the proposed EMEH. A proof-of-concept prototype of the proposed EMEH has also been designed and fabricated for the laboratory characterization testing, and field testing on a real highway bridge subjected to daily traffic vibration in New York.

Table of Contents

Executive Summary iv
Table of Contents v
List of Figures vi
List of Tables viii
Section 1. Literature Review 1
Subsection 1.1. Introduction 1
Subsection 1.2. Energy Harvesters 2
Subsection 1.3. Self-Powered Sensors 11
Section 2. Theory and Basic Concept of the EMEH 13
Subsection 2.1. Introduction 13
Subsection 2.2. Electromechanical Model 13
Subsection 2.3. Governing Equation 19
Subsection 2.4. Numerical Verification 21
Subsection 2.5. Results and Discussion 26
Section 3. Design, Fabrication, and Testing of a Proof-of-Concept Prototype 30
Subsection 3.1. Introduction 30
Subsection 3.2. Design and Fabrication of a Proof-of-Concept Prototype 30
Subsection 3.3. Laboratory Testing 31
Subsection 3.4. Field Testing 34
Section 4. Conclusions 37
References 38

List of Figures

Figure 1.1. A Wireless Strain Sensor used for Real-time and Long-term Structural Health Monitoring of Bridges (https://www.resensys.com) 2
Figure 1.2. Models of PEHs with Dynamic Magnifiers: (a) Lumped Model and (b) Distributed Cantilever Beam Model. 3
Figure 1.3. Multi-mode Double Beam Energy Harvester (Zhou et al., 2012) 4
Figure 1.4. PEH with an impact mechanism (Halim and Park, 2014). 4
Figure 1.5. Micro EMEH of the Volume 0.1 cm^3 (Beeby et al., 2007). 5
Figure 1.6. Wideband Vibration-based Micro-power Generators with Adjustable Stopper (Soliman et al., 2008). 6
Figure 1.7. Schematic Drawing of Multi-frequency FR4 EMEH (Yang et al., 2009). 6
Figure 1.8. Cross-section of a Unit Cell used in the Locally Resonant EMEH (Mikoshiba et al., 2013) 7
Figure 1.9. A Multi-frequency EMEH Design Based on Magnetic Spring Technique (Foisal et al., 2012) 8
Figure 1.10. Isometric View of a Multimodal Prototype Mechanical Hybrid Energy Harvester (Tadesse et al., 2009) 9
Figure 1.11. Different Energy Harvester Analytical Models: (a) 1DOF PEH; (b) 1DOF EMEH; (c) 2DOF PEH; (d) 2DOF EMEH; (e) 2DOF HPEMEH (Wang et al., 2014). 10
Figure 1.12. Tunable multi-frequency HPEMEH (Xu et al., 2016). 11
Figure 2.1. Configuration of the EMEH and its Key Components; (a) Vertical Cross-section of the EMEH in the XZ-plane and (b) Geometrical Parameters of the PMs Arrays in Details. 14
Figure 2.2. Electromechanical Model of the EMEH Consisting of a Lumped SDOF Dynamic System Coupled to a Lumped First Order RL Circuit. 15
Figure 2.3. Planar Arrangement of the PMs Poles in Four Different Multipole Arrays: (a) Uniform, (b) X-linear Alternating, (c) Y-linear Alternating, and (d) Planar Alternating. 16
Figure 2.4. Geometrical Parameters of the AC in Detail; (a) Cross-section in the xy-plane; (b) Cross-section in the xz-plane; and (c) the Equivalent PM of p-turn. 18
Figure 2.5. FE Model used for Validation of the Force-current Model Developed for the Proposed EMEH: (a) Longitudinal Cross-section on the XZ-Plane, (b) XY-Plane, (c) FE Model Enclosed by the Air Domain; and (d) B_{tot}-field on the XZ-plane at Y=0 for $u_{sx}=-0.216a_c$ and $I_{ci}=-0.849$ A. 22
Figure 2.6. Comparison Between the Analytical Model and the FE Model to Calculate the Magnetic Force; (a) Displacement of the AC, (b) Electric Current Induced in the AC, and (c) Magnetic Force F_{cx} Acting on the AC. 25

Figure 2.7. Variation of the Electromechanical Coupling Coefficient (EMCC) with (a) Time and (b) Displacement of the AC. 26
Figure 2.8. Electrical Power Harvested from the Simple EMEH During its First Two Cycles of Vibration. 26
Figure 2.9. Average Electrical Power Harvested from the Proposed EMEH Versus the Ratio of the Load Resistance to the Coil Resistance (R_l/R_c) for (a) PMs Array 1, (b) PMs Array 2, (c) PMs Array 3, and (d) PMs Array 4. 29
Figure 3.1. Proof-of-concept Prototype of the Proposed EMEH; (a) 3D View of the Fabricated Device in Laboratory with Details on Geometry of (b and c) the PMs Arrays and their Planar Arrangement, and (d) the Copper Coil. 31
Figure 3.2. Experimental Setup Established to Test the Proof-of-concept Prototype of the Proposed EMEH in a Laboratory Environment under Harmonic Excitations. 32
Figure 3.3. Power Spectral Density of the Acceleration of Base Recorded by an Accelerometer of the Model Data Logger X2-5. 33
Figure 3.4. Voltage Output from the Prototype EMEH Subjected to Five Different Base Excitations with the Frequencies from f_b=1.5 Hz to f_b=3.0 Hz; RMSs of these Voltage Signals are (a) 2.8 V, (b) 3.9 V, (c) 2.8 V, (d) 1.4 V, and (e) 2.2 V. 34
Figure 3.5. The Robert F. Kennedy Bridge in New York: (a) Geographical Location of the Bridge on the Google Map, and (b) View of the Suspension bridge from Ward's Island with the Testing Location Marked (Photo is taken from the Google Map). 35
Figure 3.6. Field Testing of the Proof-of-concept Prototype of the Proposed EMEH Installed on the Robert F. Kennedy Bridge in New York: (a) Placement of the Device on the Middle of a Horizontal Lateral Bracing of the Deck, and (b) Testing Setup....35
Figure 3.7. Acceleration of the Base Excitation Recorded by an Accelerometer of the Model Data Logger X2-5 During the Field Testing: (a) 5 min Time-history of the Acceleration and (b) Power Spectral Density of the Acceleration. 36
Figure 3.8. Voltage Output from the Prototype EMEH Subjected to Vibration of the Bridge. 36

List of Tables

Table 2.1. Geometrical and Material Parameters of the AC and PMs in the FE Model Developed in COMSOL Multiphysics Software (COMSOL v.5.4, 2018). 23
Table 2.2. Parameters of the SDOF Model Developed in SIMULINK (MATLAB R2017b, 2017).....24
Table 2.3. Electromechanical Parameters of the Proposed EMEH.....28

Section 1. Literature Review

Subsection 1.1. Introduction

Finding an efficient source of energy has always been a major challenge for humans on the Earth. Fossil fuels, such as coal, oil, and natural gas, have traditionally been considered as primary sources of energy. These energy sources are, however, not only nonrenewable, but are also harmful to our health and environment. A large portion of fossil fuel-derived energy is consumed by vehicles moving daily in large cities, causing significant pollution of our environment. However, the motion of vehicles through the transportation infrastructures can also be a significant source of kinetic energy, which can be harvested to power transportation system components, thereby reducing some dependence on fossil fuel-derived energy. The number of vehicles across the US has increased dramatically over the past few decades. The highway statistics shows that the average daily vehicles miles travelled in the US is more than 5000 million, representing a massive source of kinetic energy that lies unused in transportation infrastructures.

The basic concept of energy harvesting here is to exploit this unused (wasted) power by creating a fully independent generation-consumption loop (Priya and Inman, 2009). The harvested energy can be used to power sensors and electrical equipment employed in intelligent traffic monitoring systems, which are used to monitor different components of a traffic system, including vehicles, drivers, and even pedestrians (Biswas et al., 2016), or to power over-height vehicle detection systems, which can be installed on the face of the bridge and tunnel overheads to detect incoming over-height vehicle at safe stopping distance (Singhal et al., 2018). However, the most important application of the harvested energy is in the health monitoring of bridges. Many important bridges have been equipped with structural health monitoring sensors to assess the integrity of their key structural components over time. The cost of these sensors is high due to cabling work. Recently, wireless smart sensor technology has been getting attention as an economic alternative in bridges (Spencer et al., 2016). Figure 1.1 shows a wireless strain sensor installed on the web of the steel girder of a bridge. This type of sensor usually needs a couple of 1.5V AAA batteries for the operation. These batteries are usable only for a short period of time. In the long term, they need to be replaced by new ones which can be a tedious task for a network of wireless sensors installed on a very large bridge.

Figure 1.1. A Wireless Strain Sensor used for Real-time and Long-term Structural Health Monitoring of Bridges (https://www.resensys.com)

This study focuses on the development of an innovative technology for harvesting energy from bridges by through field demonstration. The proposed technology is based on electromagnetic energy harvesting to generate power wireless sensors commonly used for health monitoring of bridges.

Subsection 1.2. Energy Harvesters

This chapter reviews works carried on the development of energy harvester used to harvest electric power from vibrational energy.

Piezoelectric Energy Harvesters (PEHs) are usually smaller in size compared to other common types of energy harvesters because of their relatively higher energy density (Priya, 2007). The mechanism of PEHs is based on piezoelectric effect observed in certain materials, also called as piezoelectric materials, such as polycrystalline ceramics, textured ceramics, thin films, and polymers, that tend to generate electric charge when subjected to mechanical stress (Priya and Inman, 2009).

PEHs commonly consist of a cantilevered composite beam with one or more piezo-ceramic layers. This beam is excited at its fixed support to vibrate at its resonant frequency. A variety of analytical models have been developed to characterize the electro-mechanical behavior of PEHs that use such configuration, such as lumped parameter (SDOF) model (DuToit et al., 2005), approximated distributed parameter model (Sodano et al., 2004), and distributed parameter model considering only the first vibration mode (Chen et al., 2006). These models are approximate and may yield inaccurate results in higher modes, depending on the ratio of the tip mass to the beam mass (Erturk and Inman, 2008). Erturk and Inman (2008) presented the exact analytical solution of a cantilevered piezoelectric energy harvester by assuming that the deflection of the cantilevered beam follows the Euler–Bernoulli

assumptions for beam bending. Their work includes closed-form expressions for the voltage, current, and power outputs (Erturk and Inman, 2008).

Various techniques have been developed to increase the amount of harvested energy from PEHs, such as the technique of impedance matching between the piezoelectric harvester and the electrical load (Kong et al., 2010; Liang and Liao, 2010). However, recently, particular attention has been devoted to the enhancement of the dynamic characteristics of PEHs to amplify the amount of harvested energy from PEHs. Aldraihem and Baz (2011) have proposed a lumped mass model to study PEH with a dynamic magnifier. This model consists of a spring-mass system which is placed between the piezoelectric element and the moving base. The dynamic magnifier has been designed to increase the strain in the piezo-element in order to amplify the amount of harvested energy. The results show that with proper selection of the design parameters of the PEH, the harvested energy can be amplified by as much as 20 percent of the traditional PEHs. The effective bandwidth of the proposed PEH is wide with side bands that are about 25 percent of the resonant frequency of traditional PEHs (Aldraihem and Baz, 2011). The authors also expanded the idea of dynamic magnifier for PEHs using a distributed cantilever beam model. Figure 1.2 compares these two types of models for PEHs with dynamic magnifiers (Aladwani et al., 2014, 2012).

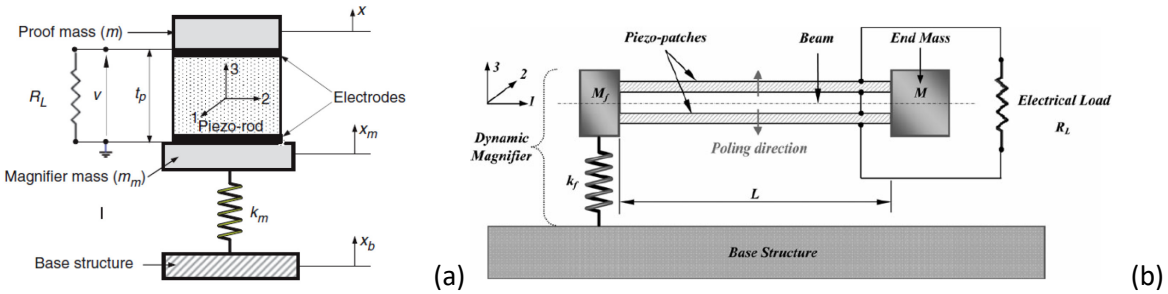

Figure 1.2. Models of PEHs with Dynamic Magnifiers: (a) Lumped Model and (b) Distributed Cantilever Beam Model.

Zhou et al. (2012) proposed a novel PEH with a multi-mode dynamic magnifier, which is capable of significantly increasing the bandwidth and the energy harvested from the ambient vibration. As shown in Figure 1.3, this PEH consists of a primary cantilever beam (primary beam) with a large tip mass at its free end, where a secondary cantilever beam with a smaller mass is attached at its free end. The secondary beam is composite with a PZT film on its surface. The primary beam acts as a dynamic magnifier here to amplify the vibration of the secondary beam which performs the energy harvesting function through the PZT film. Zhou et al. (2012) have demonstrated experimentally that adding a multi-mode dynamic magnifier can increase the harvested energy by 25.5 times in a frequency range of 3 Hz–300 Hz (Zhou et al., 2012).

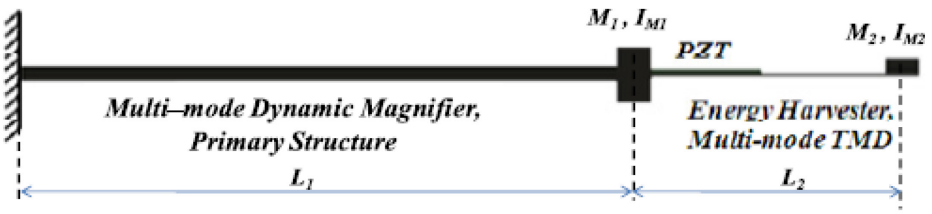

Figure 1.3. Multi-mode Double Beam Energy Harvester (Zhou et al., 2012)

The concept behind the mechanism of this PEH is based on that of tuned mass damper to suppress vibration. The idea is to tune all the modes of the harvester beam to the modes of the primary beam so that all the vibration modes of the harvester beam will be magnified by the resonances of the primary beam (Zhou et al., 2012).

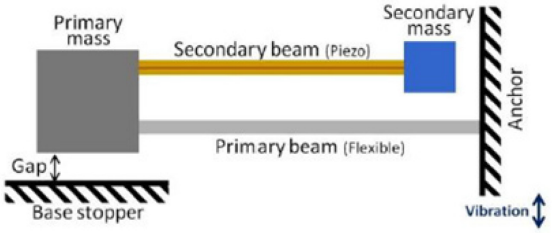

Halim and Park (2014) developed a low frequency vibration PEH with a mechanical impact mechanism designed to increase both bandwidth and output power. As shown in Figure 1.4, this PEH consists of two parts: (1) a primary cantilever beam with a mass attached to its end (2) a second cantilever beam that is stiffer and has a smaller mass at its end. The other end of the secondary cantilever beam, which plays the role of harvester, is clamped on the primary mass in a parallel manner over the primary cantilever beam that acts as a dynamic magnifier. However, these researchers in order to enhance the performance of the PEH, placed a base stopper below the primary mass with a small gap to create an impact mechanism to amplify the vibration of the system (Halim and Park, 2015, 2014). More examples of innovative techniques developed to increase the harvested energy in PEH can be found in other literature (Fu et al., 2019; X. Li et al., 2019; Nedelchev and Kralov, 2017).

Subsection 1.2.2. Electromagnetic Energy Harvesters (EMEHs)

because of the motion of the permanent magnet as per the Lenz's law (Amjadian and Agrawal, 2020, 2018, 2017).

Many studies have been carried out on small sized EMEHs with single-frequency resonance, i.e., they are tuned only to resonate with the first mode of the primary structure. For this reason, they are also called narrow band EMEHs. Many of these studies have focused on increasing the power density of EMEHs through optimization of the harvesting circuit components. El-hami et al. (2001) fabricated a high energy density electromagnetic transducer for generating electrical power from mechanical energy in a vibrating environment. The testing results showed that the EMEH prototype can generate a power of 1mW within a volume of 240 mm^3 at a resonance frequency of 320 Hz (El-hami et al., 2001). Beeby et al. (2007) developed a micro EMEH with a volume of 0.1 cm^3 optimized for a low level of ambient vibration. Figure 1.5 illustrates this micro harvester. It consists of a copper coil, four high energy density rare earth neodymium iron boron (NdFeB) magnets with the size 1×1×1.5 mm^3 bonded to the top and bottom surfaces of a cantilever beam clamped onto the base using a nut and bolt and a square washer. The harvester is capable of generating 46µW power from an ambient vibration of 60 mg with the resonant frequency of 52 Hz (Beeby et al., 2007). The energy-harvesting capability of narrow band EMEHs is limited because of their inability of being tuned to a wider frequency band of the primary structure, considering that the ambient vibration is random and naturally wideband. Optimization of these types of EMEHs is limited to the components of the harvester circuit. More researches on narrow band EMEHs can be found in the literature (Elvin and Elvin, 2011; Halim et al., 2015; Kwon et al., 2013; Liu et al., 2015; Peigney and Siegert, 2020; Salauddin et al., 2016; Zeng and Khaligh, 2013).

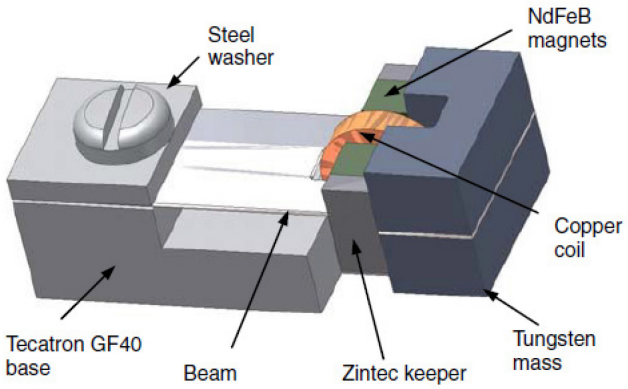

Figure 1.5. Micro EMEH of the Volume 0.1 cm^3 (Beeby et al., 2007).

Therefore, to increase the output electric power, a specific attention has been devoted to multi-frequency EMEHs, so called wide band EMEHs, in which each mode of vibration represents one resonant frequency. Soliman et al. (2008) developed a wideband micro-power generator utilizing a nonlinear vibrator, namely piecewise-linear oscillator, instead of traditional linear vibrator to as harvest energy

(See Figure 1.6). The nonlinearity is because of a stopper that can move along a track to vary the effective length of the vibrator beam when it collides with the stopper during the vibration. The stopper position can be changed to vary the stiffness of the beam and consequently the resonance frequency of the harvester (Soliman et al., 2008).

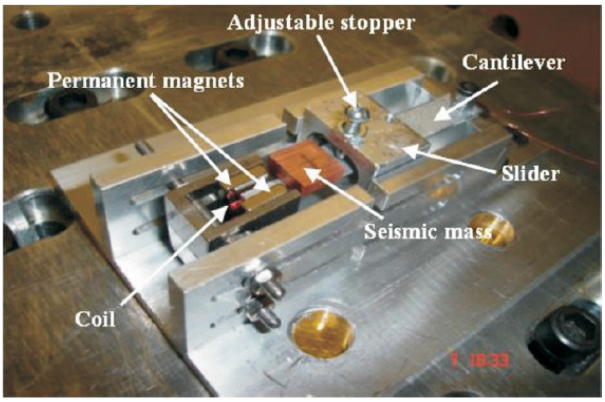

Figure 1.6. Wideband Vibration-based Micro-power Generators with Adjustable Stopper (Soliman et al., 2008).

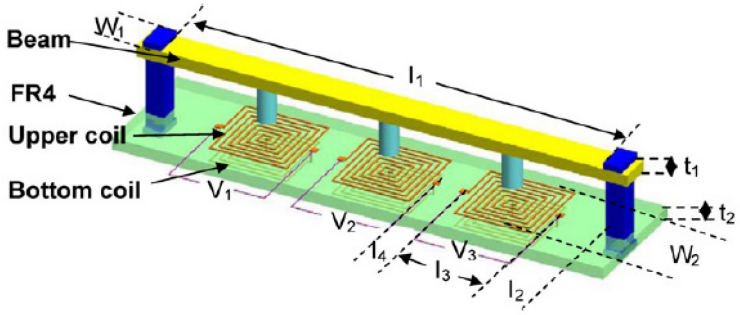

Figure 1.7. Schematic Drawing of Multi-frequency FR4 EMEH (Yang et al., 2009).

based on the theory of locally resonant materials exhibiting a band gap frequency range under vibration. The EMEH includes several unit cells attached in series, each one consisting of a spring-loaded permanent magnet moving within in a capped plastic tube enclosed by copper coils (See Figure 1.8). The test results revealed that the developed harvester can generate a peak voltage of 3.03 V, and a single cell can produce an output power of 36 mW when subjected to a harmonic excitation with a frequency close to the local resonance frequency of 140.6 Hz and an amplitude of 10 mm (Mikoshiba et al., 2013).

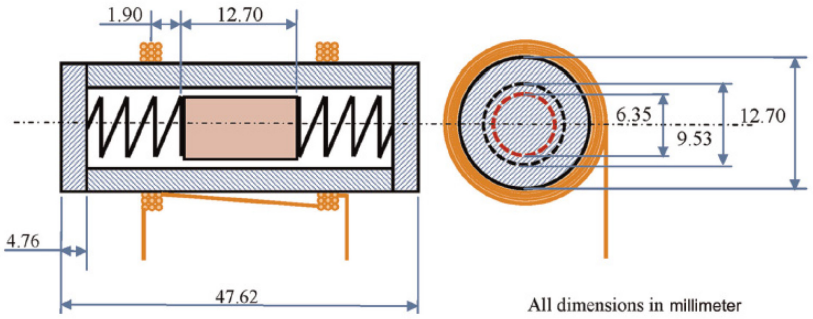

Foisal et al. (2012) fabricated a multi-frequency EMEH desinged based on magnetic spring technique. This EMEH consists of four power generators in series as shon in Figure 1.9. Each genrator consists of two stationary end permanent magnets fixed at the top and bottom of the cylinder. A moving middle permanent magnet is loactaed between the two fixed permanent magnets in the way that the similar poles face each other (Foisal et al., 2012).

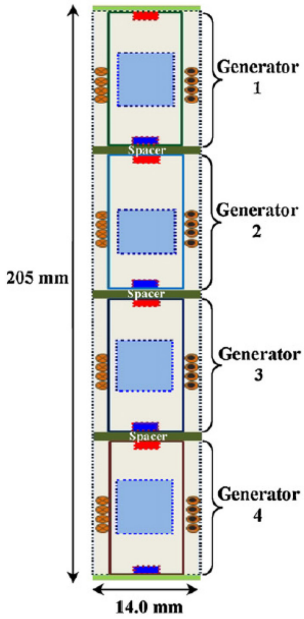

The magnetic repulsive interaction between the moving and stationary permanent magnets creates a magnetic spring to provide restoring force in the mechanichal system. The motion of the middle permanent magnet with respect to a coil surronding the clylinder induces an AC voltage in the harvester circuit. The experimental results show that the EMEH can operate in the 7–10 Hz frequency range with a power density of 52.02 µW/cm3 when s to an acceleration of 0.5g (Foisal et al., 2012).

Subsection 1.2.3. Hybrid Piezoelectric-Electromagnetic Energy Harvesters (HPEMEH)

There are also few research works in which PEHs and EMEHs have been combined to harvest vibration energy. These types of energy harvesters are called hybrid piezoelectric-electromagnetic energy harvesters (HPEMEH).

Tadesse et al. (2009) developed a HPEMEH combining the energy harvesting from piezoelectric and electromagnetic mechanisms on the same platform (Tadesse et al., 2009). This system consists of piezoelectric crystals bonded to a cantilever beam and a permanent magnet attached to the tip of the cantilever beam as shown in Figure 1.10.

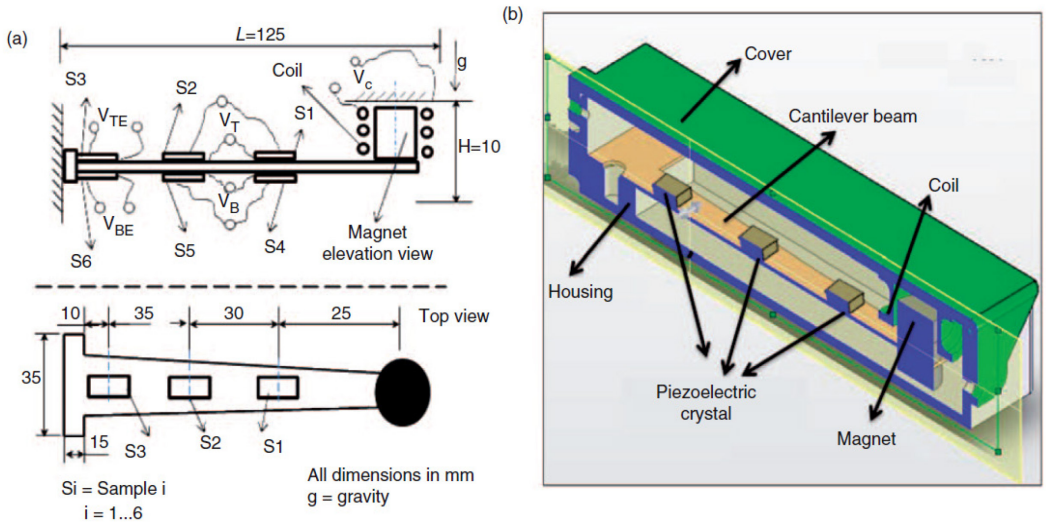

The permanent magnet oscillates within a stationary coil fixed to the top of the platform. The permanent magnet has two significant roles: (1) acting as a tip mass for the cantilever beam to reduce the resonance frequency, and (2) acting as a moving magnetic source to induce electric current in the stationary coil as per Faraday's law (Tadesse et al., 2009). It was found that combining the two mechanisms together improves the performance of the system over a wide frequency range. The electromagnetic part is capable of generating a high electric power at low frequencies, while the piezoelectric part is capable of generating a high electric power at high frequencies. The peak electric power generated by the electromagnetic mechanism found to be 0.25 W at 20 Hz frequency and that generated by the piezoelectric mechanism was found to be 0.25 mW for the same frequency (Tadesse et al., 2009).

Wang et al. (2014) developed a 2DOF HPEMEH aimed at not only achieving wider bandwidth, but also an increased electric power by combining piezoelectric and electromagnetic mechanisms of comparable macroscopic size (Wang et al., 2014). The peak electric power of the 2DOF HPEMEH was compared both experimentally and theoretically to those of the 1DOF PEH, 1DOF EMEH, 2DOF PEH, and 2DOF EMEH.

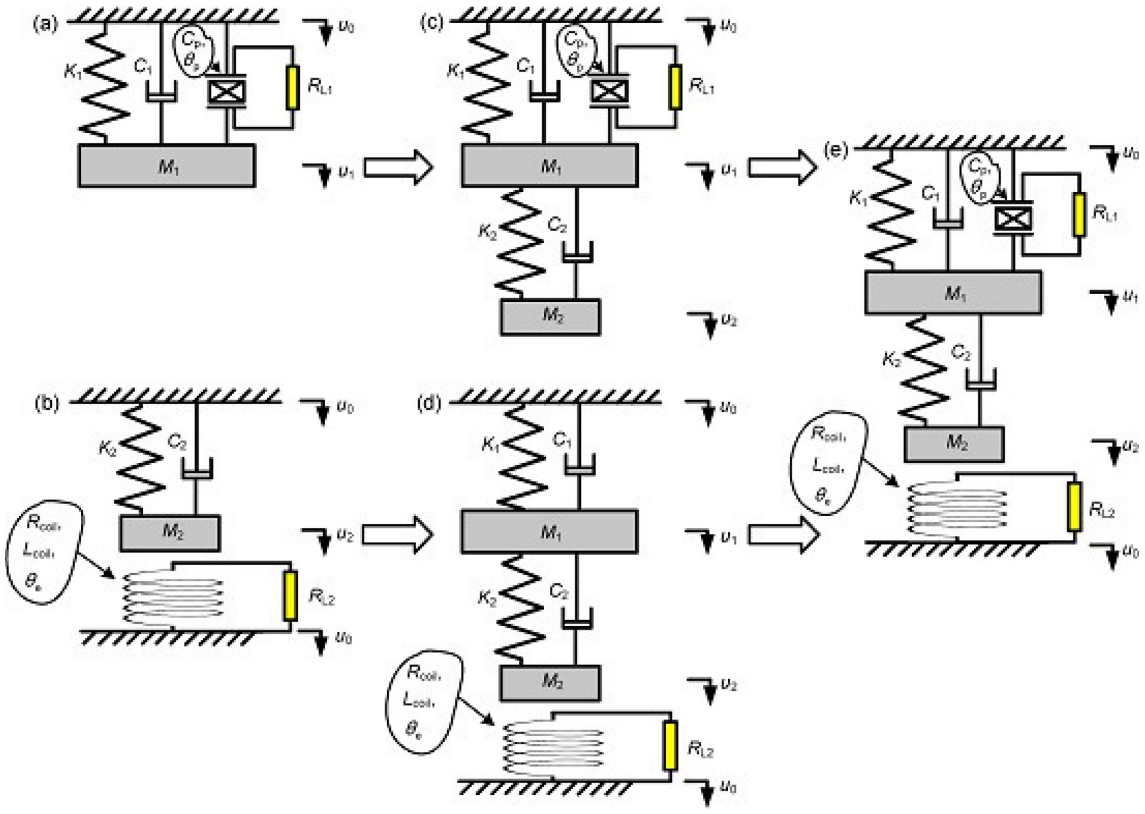

Figure 1.11 compares the analytical models of these energy harvesters. The authors found that although the increase of the electric power output from one electromechanical transducer will lead to the decrease of the electric power output from the other, the total electric power output of the 2DOF HPEMEH model increases (Wang et al., 2014).

Xu et al. (2016) developed a novel tunable multi-frequency HPEMEH in which a PEH is coupled to an EMEH with magnetic interaction. This hybrid harvester consists of a cantilevered piezoelectric beam with a cylindrical permanent magnet as a proof mass and a lower permanent magnet moving inside a stationary coil as shown in Figure 1.12 (Xu et al., 2016).

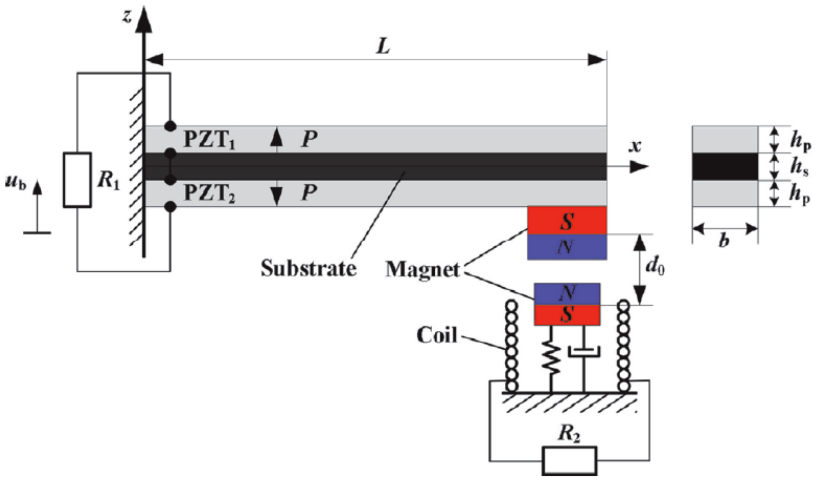

The repulsive magnetic interaction between the two permanent magnets couples the vibration of the beam to the motion of the lower permanent magnet. Under an external excitation, the mechanical strain is converted into voltage in the piezoelectric layers, and the relative motion between the lower permanent magnet and coil induces a current voltage in the harvesting circuit as per Faraday's law. The experimental results show that the measured first peak power increases by 16.7% and 833.3% compared to that of the multi-frequency EMEH and the multi-frequency PEH, respectively (Xu et al., 2016).

Subsection 1.3. Self-Powered Sensors

A review of the previous works carried out on energy harvesters discussed above shows that piezoelectric mechanism is more promising for micro-scale vibration energy harvesters. However, electromagnetic mechanism provides the highest levels of performance when size is not an issue and conventional discrete coils and magnets can be employed (Jung et al., 2011; Priya and Inman, 2009). From this review, it can be also concluded that the performance of an EMEH for powering sensors can be improved by:

- Optimizing the geometrical and electrical properties of components of the electrical part such as the size of the permanent magnet and coil, and the ratio of load resistance to coil resistance (R_l/R_c).
- Optimizing the geometrical and dynamical properties of components of the mechanical parts, such as the value of mass, stiffness, and damping leading to tuning of the natural frequency of energy harvester to the frequency of the first mode of the primary structure to create resonance in the energy harvester.

- Increasing the number of resonant frequencies of the energy harvester to harvest energy over a wider frequency band by adding additional mass to system or creating an impact mechanism to change stiffness.
- Combining the EMEH with a PEH to create a hybrid energy harvester with higher energy density.

A typical electronic device (e.g. sensor) consuming 100 µW of power on average from a 1 cm^3 of non-rechargeable lithium battery can be operational for approximately 1 year. This lifetime is not practical for long-term monitoring of structural response, for example, of long bridges during their service lives. The development of self-powered sensors by generating or harvesting energy from the vibrational energy is the most efficient and practical method to solve this issue. A study on the use of 8 nodes of wireless sensors for monitoring of a cable-stayed bridge showed that voltage levels of the rechargeable batteries of the sensors stayed around 4.15V during 1.5 months of monitoring. This reveals that EMEHs have this capability to continuously charge rechargeable batteries for powering wireless sensors installed on bridges for a quite long time (Cho et al., 2010).

Li and Pillay (2007) developed an EMEH to harvest vibration energy in bridges and use it as 3.3V power supply for wireless sensors. Laboratory testing of a prototype of the EMEH showed that it can generate enough power for wireless sensors (Haodong and Pillay, 2007). These researchers later tested an improved version of the EMEH to develop a self-powered wireless sensor system that can be used on bridges for a variety of monitoring tasks in the long term. It was found that the proposed EMEH can effectively harvest up to 12.5 mW of eletric power from a typical bridge at the resonant frequency 3.1 Hz (Sazonov et al., 2009). Jung et al. (2011) developed an electromagnetic energy harvester that utilizes the wind-induced vibration of a stay cables and investigated its feasibility for powering a wireless sensor node placed on the cable. The results showed that the device is capable of generating a peak power of 233.49 mW and an RMS power of 27.14mW under the peak input acceleration 74.8mg. It was verified that the proposed energy harvesting system can generate sufficient power for the wireless sensor node under the moderate wind condition (Jung et al., 2011). Asadi et al. (2017) studied a nano plate self-powered sensor based on electromagnetism mechanism. This self-powered sensor consists of a moving small permanent magnet mounted on a nano plate, and a stationary coil. The authors investigated the capacity of sensor in linear and non-linear cases under different excitations through finite element simulation. The results showed that the resonance frequency of sensor is 330 MHz, and for a gap of 1.5 nm, it can generates 1.7 and 2.24 mW/cm^3 for linear and nonlinear cases, respectively (Asadi et al., 2017). Li et al. (2019) proposed an impact based EMEH with arrays of magnet and coil for accumulating energy and powering wireless sensor nodes. They derived a model for the nonlinear interface circuit that is able to function even if the stored energy is completely drained. Experimental results indicated that the charging efficiencies of the proposed circuit are 172% and 28.5% higher than that of the conventional EMEH circuits for external excitations of 0.3g and 0.4g, respectively, at 8 Hz frequency (K. Li et al., 2019).

Section 2. Theory and Basic Concept of the EMEH

Subsection 2.1. Introduction

This chapter focuses on the theory behind the mechanism of the EMEH. An electromechanical model is presented to evaluate the performance of the EMEH to harvest electrical energy from traffic vibration.

Subsection 2.2. Electromechanical Model

Figure 2.1(a) illustrates the configuration of the proposed EMEH consisting of a thick rectangular air-core copper coil (AC) moving relative to two identical planar arrays of permanent magnets (PMs) located on its left and right sides. The PMs arrays are firmly fastened to a base (primary structure) moving with the displacement $u_{bX}(t)$ along the X-axis. They are mounted inside two housings made of a non-magnetic material. The AC is attached to the base through a system of elastic spring and viscous damper. The size of the vertical air gap between the AC and the left and right PMs arrays along the Z-axis is denoted by Δ_{gZ}. Figure 2.1(b) shows the plan of the left and right PMs arrays in the XY-plane. Each PMs array consists of $n=n_X \times n_Y$ cuboidal PMs of the size $a_m \times a_m \times a_m$ which are separated from each other through air-gaps of the size δ_{gmX} and δ_{gmY} along the X and Y-axes, respectively. Therefore, the dimensions of the left and right PMs arrays would be $L_m=n_X a_m+(n_X-1)\delta_{gmX}$, $W_m=n_Y a_m+(n_Y-1)\delta_{gmY}$, and $H_m=a_m$.

Electric power is harvested from the EMEH by connecting the AC to a series electrical load representing the resistance of the harvesting circuit. The harvested electric power is generated by the electromagnetic induction occurring in the AC when it moves relative to the left and right PMs arrays. This relative motion causes a change in the magnetic flux of the PMs passing through the AC and induces an electromotive force in the circuit as per the Faraday's law of induction. This results in the electric current $I_{ci}(t)$ flowing in the copper wire of the AC whose direction varies with the motion of the AC. The direction of this electric current changes as per the Lenz's law in such a way that the induced magnetic field opposes the initial cause of change in the magnetic flux of the PMs which is the motion of the AC. Eventually, this interaction causes the braking (damping) force F_c that acts on the AC and its direction that is always opposite to the direction of the velocity of the AC, i.e. $\dot{u}_{sX}(t)$.

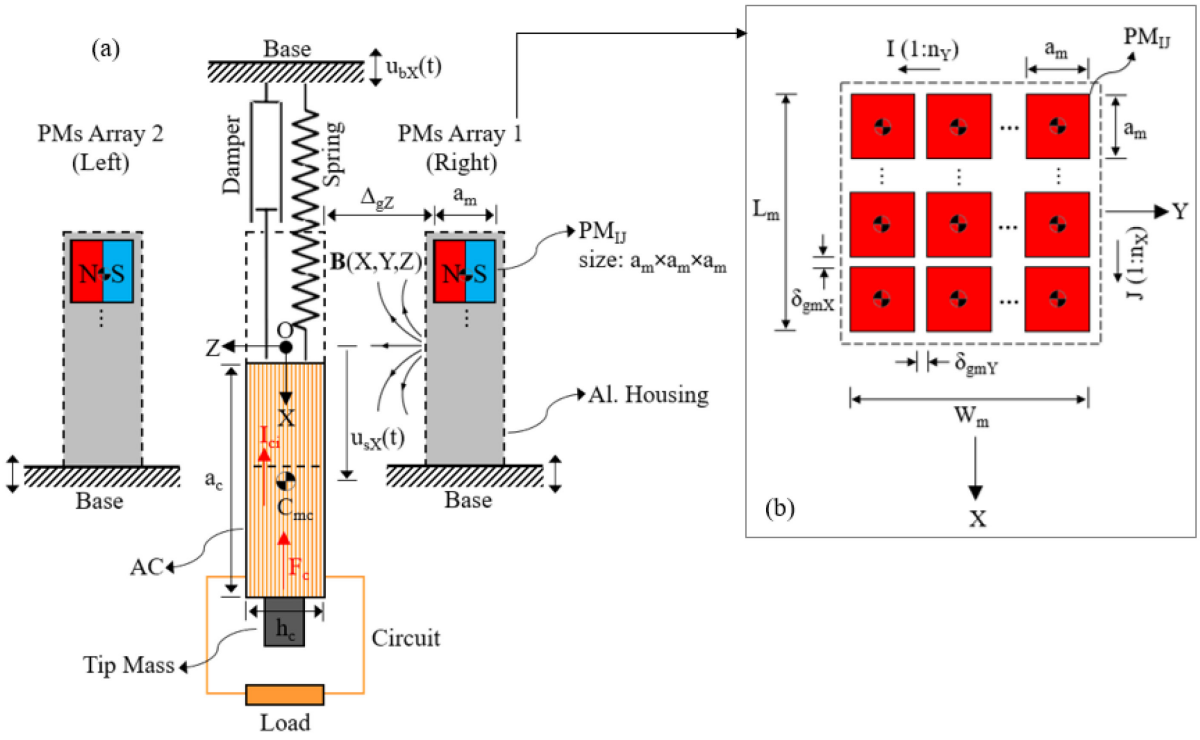

The harvested electric power can be increased by amplifying the amplitude of the vibration of the AC in the magnetic field of the PMs. This can be done by matching the natural frequency of the AC to that of the base excitation. For this purpose, a tip mass is attached to the AC to vary the natural frequency of the AC.

The proposed EMEH can be modeled as a linear single-degree-of-freedom (SDOF) system coupled with a series alternating-current RL circuit as shown in Figure 2.2.

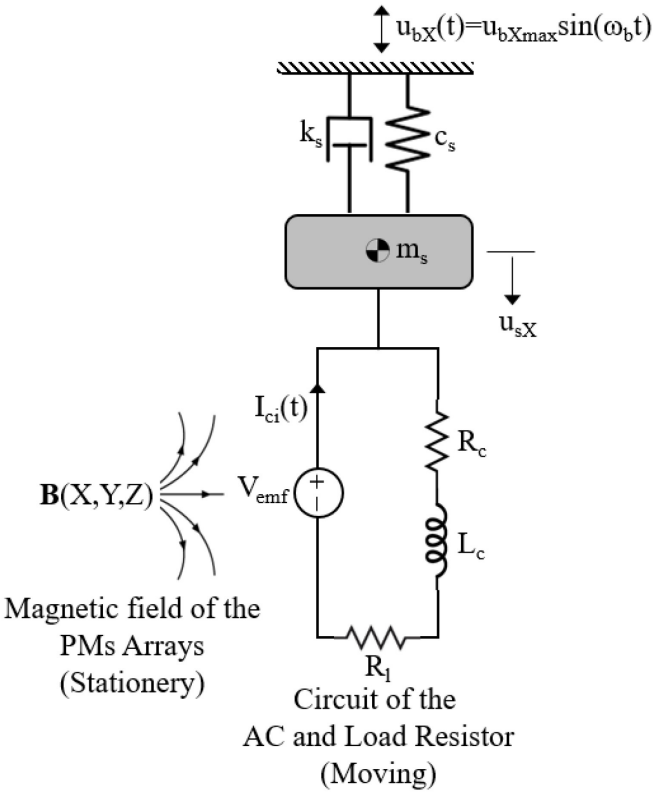

The SDOF system is subjected to the base excitation $u_{bX}(t)=u_{bXmax}\sin(\omega_b t)$ along the X-axis where u_{bXmax} and $\omega_b=2\pi f_b$ are the amplitude and the circular frequency of the excitation, and f_b being the frequency of the excitation. The stiffness and mechanical damping coefficients of the elastic spring and viscous damper are denoted by k_s and c_s, respectively. The total mass of the SDOF system, consisting of the mass of the AC and the tip mass, is denoted by m_s. The degree of freedom of the SDOF system is also denoted by u_{sX} which represents the displacement of the mass center of the AC.

The RL circuit consists of two resistors R_c and R_l, and an inductor L_c connected in series to an altering-voltage source with the electromotive force $V_{emf}(t)$. R_c and L_c represent the resistance and induction of the AC, respectively, and R_l is the resistance of the electrical load used to harvest the electric power.

Subsection 2.2.1. Planar Arrangement of the PMs

The arrangement of the PMs based on the magnetic direction of their poles is an important feature of the EMEH that can affect the magnetic interaction of the PMs with the AC.

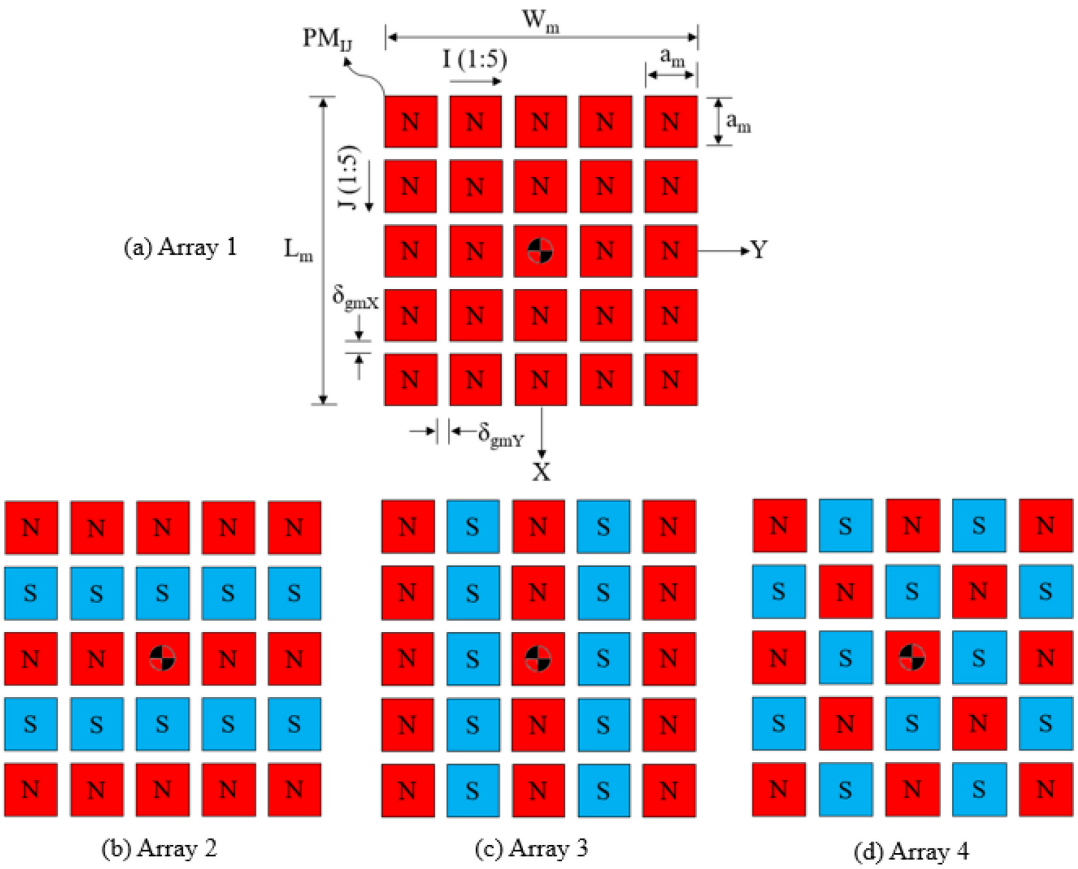

Figure 2.3 shows the planar arrangement of the PMs poles in four different multipole arrays including: (1) uniform, (2) X-linear alternating, (3) Y-linear alternating, and (4) planar alternating. It is assumed that n_X=5 and n_Y=5. The arrays, therefore, consist of 25 identical cubic PMs with the side length $a_{m,}$ which are separated from each other by air-gaps of the size δ_{gmX} and δ_{gmY} along the X and Y-axes, respectively.

It is seen that Arrays 3 is created by 90° rotation of Arrays 2. The magnetic interaction of Array 3 with the AC is however different than that of Array 2 because the magnetic flux densities of the PMs in these two arrays have different angles with the direction of the motion, which can strongly affect the strength of the induced electric current flowing the copper wire of the AC (Amjadian and Agrawal, 2018, 2017).

The magnetic flux density vector of each of the left ($\mathbf{B}_L$) and right ($\mathbf{B}_R$) PMs arrays shown in Figure 2.1(a) can be calculated by summing up the magnetic flux density vectors of the PMs as follows,

$$\boldsymbol{B} = \sum_{I=1}^{n_Y} \sum_{J=1}^{n_X} \boldsymbol{B}_{IJ} \qquad (2\text{-}1a)$$

where $\mathbf{B}_{IJ}$ is the magnetic flux density vectors of the IJ-th PM given by,

$$\boldsymbol{B}_{IJ} = -\frac{1}{4\pi} B_{rmIJ} \sum_{i,j,k=1}^{2} (-1)^{i+j+k} \boldsymbol{b}(X - X_{cIJi}, Y - Y_{cIJj}, Z - Z_{cIJk}) \qquad (2\text{-}1b)$$

in which $X=X_{cIJ1}$, $X=X_{cIJ2}$, $Y=Y_{cIJ1}$, $Y=Y_{cIJ2}$, $Z=Z_{cIJ1}$, and $Z=Z_{cIJ2}$ are the coordinates of the boundary surfaces surrounding the volume of the IJ-th PM with respect to the X-, Y-, and Z-axes, respectively, and $B_{rmIJ}=\lambda_{mIJ}B_{rm}$ in which B_{rm} is the magnetic remanence of that PM and λ_{mIJ} is the direction coefficient representing the direction of the magnetization vector. $\lambda_{mIJ}=+1$ for $\mathbf{M}_{rmIJ}=+(B_{rm}/\mu_0)\mathbf{e}_Z$ implying that N-pole faces the XY-plane in the positive direction of Z-axis and $\lambda_{mIJ}=-1$ for $\mathbf{M}_{rmIJ}=-(B_{rm}/\mu_0)\mathbf{e}_Z$ implying that S-pole faces the XY-plane in the positive direction of Z-axis. Note that $\mu_0=4\pi\times10^{-7}$ Tm/A is the magnetic permeability of the vacuum. The rectangular components of the vector $\mathbf{b}=b_x\mathbf{e}_x+b_y\mathbf{e}_y+b_z\mathbf{e}_z$ in Equation (2-1b) are defined as (Amjadian and Agrawal, 2017),

$$b_X = ln(Y+R),\ b_Y = ln(X+R),\ b_Z = tan^{-1}\left(\frac{YZ}{XR}\right) + t\,an^{-1}\left(\frac{XZ}{YR}\right) \qquad (2\text{-}1c)$$

in which $R=(X^2+Y^2+Z^2)^{1/2}$.

Subsection 2.2.2. Thick Rectangular Air-Core Coil (AC)

Figures 2.4(a) and 2.4(b) show the horizontal and vertical cross-sections of the AC demonstrating its key geometrical parameters. The AC has the dimensions $a_c\times a_c\times h_c$, the winding depth t_c, and the total number of turns $N_c=N_z\times N_t$, where N_z and N_t are the numbers of turns along the z-axis and the depth of the winding, respectively. It is ideally assumed that $N_z=h_c/d_w$ and $N_t=t_c/d_w$ where d_w is the diameter of the winding wire made of copper. It is assumed that $I_{ci}(t)>0$ when the electric current $I_{ci}(t)$ is counterclockwise in the xy-plane so that the N- and S-poles are established at $z=+h_c/2$ and $z=-h_c/2$, respectively, otherwise $I_{ci}(t)<0$.

The common method to calculate the magnetic field of a single-layer turn air-core coil with the surface current density $\mathbf{K}'_{bm}$ is to approximate it by the magnetic field of an equivalent PM of the same dimensions as shown in Figure 2.4(c). The magnetization vector $\mathbf{M}'_{rm}$ of the equivalent PM is related to $\mathbf{K}'_{bm}$ through $\mathbf{K}'_{bm}=\mathbf{M}'_{rm}\times\mathbf{n}$, where $\mathbf{n}$ is the unit surface normal vector of the equivalent PM (Furlani, 2001). The Shell Method (Robertson et al., 2012) can be used to model a multi-layer turn air-core coil referred to as the thick rectangular air-core coil (AC) in this study. This method treats each single layer of turn as an equivalent cuboidal PM of the dimension $a'_{mq}\times a'_{mq}\times h'_{mq}$ where $a'_{mq}=a_c-[2(N_t-q)-1]d_w$ and $h'_{mq}=h_c$. The magnetic remanence of this PM is $B'_{rm}=\mu_0(N_zI_{ci}/h_c)$ where $B'_{rm}=\mu_0M'_{rm}$ and $I_{ci}=(h_cK'_{bm})/N_z$.

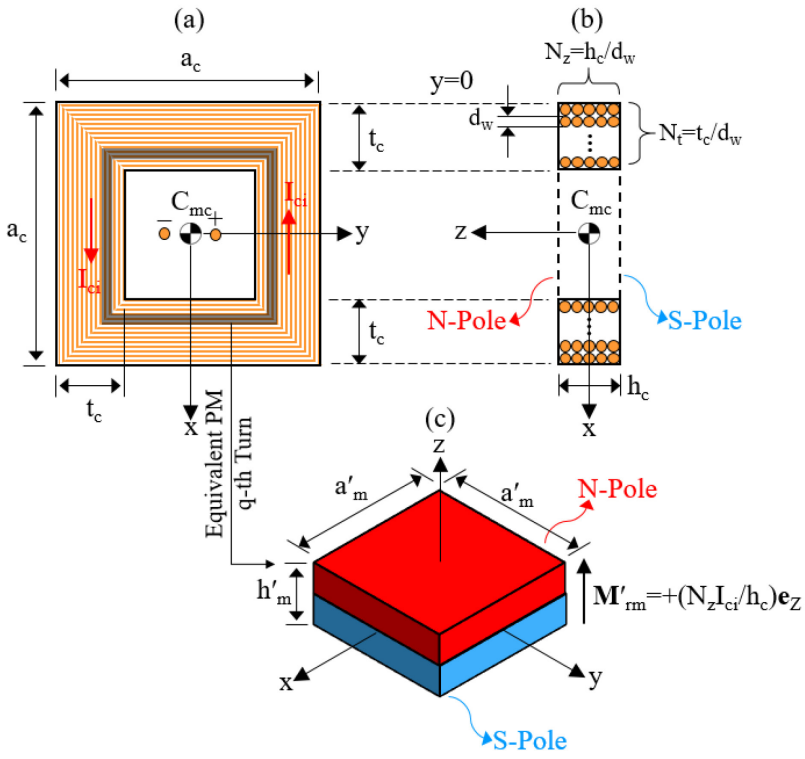

The magnetic field of the AC can be calculated by superposing the magnetic fields of all the equivalent cuboidal PMs as follows,

$$\boldsymbol{B}_c = \sum_{q=1}^{N_t} \boldsymbol{B}_{cq} \qquad (2\text{-}2)$$

where $\mathbf{B}_{cq}$ is the magnetic flux density vector of the q-th turn of the AC that is calculated by Equation (2-1) for $n_X=n_Y=1$ as per the Shell Method (Robertson et al., 2012). The resistance of the AC is given by,

$$R_c = \frac{l_w}{\sigma_c A_w} \qquad (2\text{-}3)$$

in which $l_w=4N_zN_t(a_c-t_c)$, $\sigma_c=58.58$ MS/m, and $A_w = \pi d_w^2/4$ are the length, electrical conductivity, and cross section area of the winding copper wire, respectively. The inductance of the AC is also given by (Paul, 2009),

$$L_c = 2\frac{\mu_0}{\pi} N_z^2 \sum_{q=1}^{N_t} a_{cq}\left[\ln\left(\frac{a_{cq}}{d_w}\right) - 0.0809\right] \qquad (2\text{-}4)$$

where $a_{cq}=a_c-2(N_t-q)d_w$ is the length of the sides of q-th turn.

Subsection 2.2.3. Magnetic Interaction Between the AC and the PMs Arrays

The magnetic force applied to the AC when subjected to the magnetic field of each of the left ($\mathbf{F}_{cL}$) and right ($\mathbf{F}_{cR}$) PMs arrays is given by,

$$\boldsymbol{F}_c = \sum_{I=1}^{n_Y}\sum_{J=1}^{n_X}\boldsymbol{F}_{cIJ} \qquad (2\text{-}5a)$$

where $\mathbf{F}_{cIJ}$ is the magnetic force applied to the AC due to the magnetic field of the IJ-th PM that is calculated using the Shell Method and is given by (Robertson et al., 2012),

$$\boldsymbol{F}_{cIJ} = \sum_{q=1}^{N_t}\boldsymbol{F}'_{mIJq} \qquad (2\text{-}5b)$$

where $\mathbf{F}'_{mIJq}$ is the magnetic force applied to the q-th turn of the AC due to the magnetic field of the IJ-th PM that is given by (Amjadian and Agrawal, 2018, 2017),

$$\boldsymbol{F}'_{mIJq} = \frac{1}{16\pi\mu_0}B_{rmIJ}B'_{rm}V'^{\frac{2}{3}}_{mq}\boldsymbol{f}_{mIJq}\left(\alpha'_{mq},\frac{\Delta X'_{mIJq}}{a'_{mq}},\frac{\Delta Y'_{mIJq}}{a'_{mq}},\frac{\Delta Z'_{mIJq}}{h'_{mq}}\right) \qquad (2\text{-}5c)$$

where V'_{mq} is the volume of the equivalent cuboidal PM enclosed by the q-th turn of the AC and $\mathbf{f}_{mIJq}(.)$ is a dimensionless vector function taking the effects of the following parameters into account: $\alpha'_{mq}=a'_{mq}/h'_{mq}$, where $a'_{mq}=a_c-(2q-1)d_w$, $h'_{mq}=h_c$, and the mass center eccentricity ratios $\Delta X_{mIJq}/a'_{mq}$, $\Delta Y_{mIJq}/a'_{mq}$, and $\Delta Z_{mIJq}/h'_{mq}$ along the X-, Y-, and Z-axes, respectively, where $\Delta(.)'_{mIJq}=(.)_{mIJ}-(.)'_{mq}$.

Subsection 2.3. Governing Equation

The motion of the AC when subjected to the magnetic field of the left and right PM$_S$ arrays with the magnetic flux density $\mathbf{B}_{tot}=\mathbf{B}_L(X,Y,Z)+\mathbf{B}_R(X,Y,Z)$ is described by the following two-degrees-of-freedom coupled electromechanical equation:

$$m_s\ddot{u}_{sX}(t)+c_s\dot{u}_{sX}(t)+k_su_{sX}(t)-F_{cXtot}(t)=-m_s\ddot{u}_{Xb}(t) \qquad (2\text{-}6a)$$

$$(R_l+R_c)I_{ci}(t)+L_c\dot{I}_{ci}(t)=V_{emf}(t) \qquad (2\text{-}6b)$$

where F_{cXtot} is the X-component of the total magnetic force applied to AC, i.e., $\mathbf{F}_{ctot}=\mathbf{F}_{cL}+\mathbf{F}_{cR}$ in which $\mathbf{F}_{cL}$ and $\mathbf{F}_{cR}$ can be calculated by Equation (2-5). This force can alternatively be calculated by the Lorentz force for a current-carrying wire in electromagnetism as follows,

$$F_{cXtot}=I_{ci}\oint_{coil}(d\boldsymbol{l}\times\boldsymbol{B}_{tot})\boldsymbol{e}_X \qquad (2\text{-}7a)$$

where the line integration is taken over the length of the copper wire of the AC. Here, it should be noted that the direction of this force is always apposite to the direction of the velocity of the AC, i.e., $F_{cXtot}=-c_e\dot{u}_{Xs}$ where c_e is the electrical damping caused by the magnetic interaction between the AC and the PMs arrays. The correct sign of this force is implicit in Equation (2-7a). It can be shown that,

$$F_{cXtot} = -K_f I_{ci} \qquad (2\text{-}7b)$$

where K_f is called electromechanical coupling coefficient (EMCC) or transformation factor (El-hami et al., 2001) given as,

$$K_f = \oint_{coil} (\boldsymbol{B}_{tot} \times d\boldsymbol{l}) \boldsymbol{e}_X \qquad (2\text{-}8)$$

This coefficient is time-varying because the limits of integration in Equation (2-8) changes with the motion of the AC. If we calculate F_{cXtot} using Equation (2-5) then EMCC can be calculated by Equation (2-7b) as $K_f=F_{cXtot}$ for $I_{ci}=-1$ A. However, a quite large number of researchers (Beeby et al., 2007; Shen et al., 2018; Williams and Yates, 1996; Zhu et al., 2012; Zuo and Cui, 2013) have assumed that EMCC is constant and does not change with time, i.e. $K_f=N_z B_{avg}(a_c-t_c)$ where B_{totavg} is the volume average of the magnetic flux density vector of the left and right PMs arrays over the air gap between them. This is an oversimplified assumption that may lead to error in estimation of the harvested electric power (Cannarella et al., 2011; Mösch and Fischerauer, 2019). This error is lowest for thin air-core copper coils placed in a narrow air gap.

The electromotive force V_{emf} is given by the following integral taken over the length of the AC,

$$V_{emf} = \dot{u}_{Xs}\left[\int_{coil} (\boldsymbol{e}_X \times \boldsymbol{B}_{ext})\, d\boldsymbol{l}\right] \qquad (2\text{-}9a)$$

If we manipulate the triple product under the integral and compare it with Equation (2-8), we can conclude that,

$$V_{emf} = +K_f \dot{u}_{sX} \qquad (2\text{-}9b)$$

which shows that how the generation of the induced alternating voltage in the AC is coupled to the velocity of the AC and its magnetic interaction with the left and right PMs arrays. Therefore, the relationship between the induced electric current $I_{ci}=V_{emf}/(R_l+R_c)$ and the velocity of the AC can be obtained as,

$$I_{ci} = \frac{K_f}{R_l+R_c}\dot{u}_{Xs} \qquad (2\text{-}10)$$

This equation can be used to simplify the electromechanical equation by eliminating I_{ci} from Equation (2-6) as follows;

$$m_s\ddot{u}_{sX}(t) + [c_s + c_e] + \dot{u}_{sX}(t) + k_s u_{sX}(t) = -m_s\ddot{u}_{bX}(t) \qquad (2\text{-}11a)$$

in which c_e is the electrical damping and is given by,

$$c_e = \frac{K_f^2}{R_l + R_c} \qquad (2\text{-}11b)$$

If we substitute for $u_{bX}(t) = u_{bXmax}\sin(\omega_b t)$ in Equation (2-11) and then divide the two sides of the equation by m_s we get,

$$\ddot{u}_{sX}(t) + 2\left(\xi_s + \frac{K_f^2}{2m_s\omega_s(R_l+R_c)}\right)\omega_s\dot{u}_{sX}(t) + \omega_s^2 u_{sX}(t) = \ddot{u}_{bXmax}\sin(\omega_b t) \qquad (2\text{-}12a)$$

in which $\ddot{u}_{bXmax} = \omega_b^2 u_{bXmax}$ is the maximum acceleration of the base and ξ_s is the critical mechanical damping ratio defined as,

$$\xi_s = \frac{c_s}{2m_s\omega_s} \qquad (2\text{-}12b)$$

The electrical power harvested from the EMEH is equal to the instantaneous power consumed by the load, which is given by,

$$P_l = R_l I_{ci}^2 \qquad (2\text{-}13a)$$

If we substitute for I_{ci} from Equation (2-10) we get,

$$P_l = \frac{R_l}{(R_l+R_c)^2} K_f^2 \dot{u}_{sX}^2 \qquad (2\text{-}13b)$$

where $\dot{u}_{sX}$ is the velocity of the SDOF system described by Equation (2-12). The average power over the time interval [0,τ] is given by,

$$P_{lavg} = \frac{1}{\tau}\int_0^\tau P_l(t)dt \qquad (2\text{-}13c)$$

Subsection 2.4. Numerical Verification

Three-dimensional finite element (FE) model of a simple EMEH is developed in COMSOL Multiphysics software (COMSOL v.5.4, 2018) to verify the accuracy of the Equations (2-5) and (2-7). This simple EMEH consists of an AC located in the vicinity of two identical PMs. The AC has the dimensions 1 in×1 in×0.5 in and the winding depth t_c=0.25 in and has been wound by a copper wire of 18-AWG with $d_w \cong 1$ mm and the ampacity current 16 A (Sams, 1986). The PMs have the dimensions 1 in×1 in×0.5 in and the magnetic remanence B_{rm}=1.4 T (Neodymium type N52). The size of the vertical gap between the AC and the PMs is Δ_{gcz}=0.25 in. Figures 2.4(a) and (b) show this model and the details of the meshing.

Figure 2.4(c) shows that the AC and PMs are enclosed by a sphere of the radius r_a=6 in as the air domain whose center is positioned at the origin of the XYZ coordinate system which is located at the center of the air gap between the PMs. Table 2.1 shows geometrical and material parameters of the FE model.

This problem is stationary, implying that the electric current flowing through the AC, denoted by I_{ci}, is not time dependent. Therefore, the attractive magnetic interaction between the AC and the PMs can be described by the magnetostatic form of the Maxwell's equations in the presence of an external current as follows (Furlani, 2001),

$$\nabla \times \left(\frac{1}{\mu_m}\nabla \times \boldsymbol{A}\right) = \boldsymbol{J}_e \quad , \quad \boldsymbol{B}_{total} = \nabla \times \boldsymbol{A} \qquad (2\text{-}14)$$

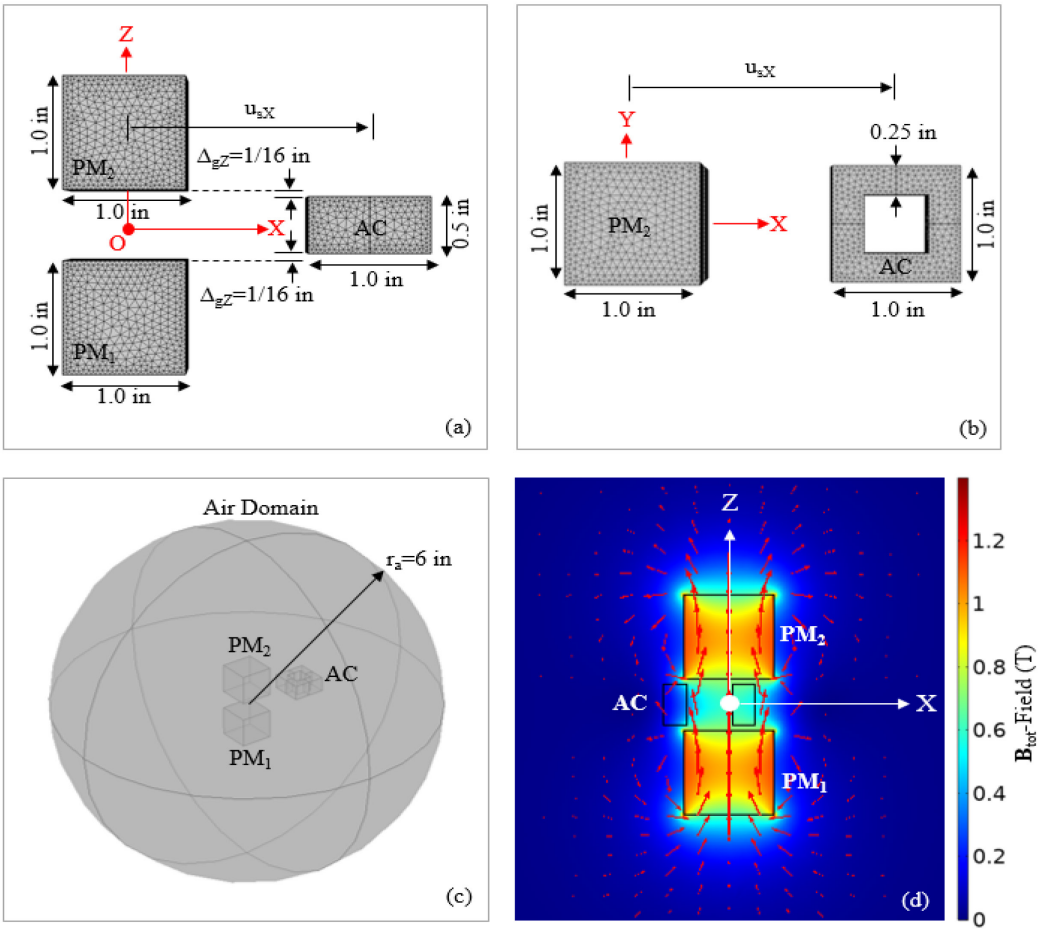

Figure 2.5. FE Model used for Validation of the Force-current Model Developed for the Proposed EMEH: (a) Longitudinal Cross-section on the XZ-Plane, (b) XY-Plane, (c) FE Model Enclosed by the Air Domain; and (d) B_{tot}-field on the XZ-plane at Y=0 for u_{sX}=−0.216a_c and I_{ci}=−0.849 A.

where **A** is the magnetic vector potential, $\mathbf{J}_e$ is the volume density vector of the electric current, and μ_m is the magnetic permeability of the materials including the PMs ($\mu_m \cong \mu_0$) and air domain ($\mu_m = \mu_0$). Equation (2-14) can be solved by an stationary solver in COMSOL multiphysics software (COMSOL v.5.4, 2018). This is carried out by satisficing the magnetic insulation boundary conditions and the equation $\nabla \bullet \mathbf{A} = 0$, which is well known as the Coulomb gauge. The magnetic force acting on the AC can also be calculated using the Maxwell stress tensor (Amjadian and Agrawal, 2019, 2018, 2017). To achieve more accurate results, it is essential to use very fine mesh along the edges of the AC and PMs as shown in Figures 2.4(a) and (b). Figure 2.5(d) shows the magnetic flux density field of the PMs on the XZ-plane at Y=0 calculated by the FE model for $u_{sX} = -0.216a_c$ and $I_{ci} = -0.849$ A. The magnetic flux density field of the AC is negligible.

Parameter	Value	Unit	Description
a_m	1	in	Length of the sides of the PMs
a_c	1	in	Length of the sides of the AC
h_c	0.5	in	Height of the AC (N_z=13)
t_c	0.25	in	Winding depth (N_t=6)
d_w	1	mm	Diameter of the copper wire (18-AWG)
Δ_{gcZ}	1/16	in	Size of the vertical gap between the AC and the PMs
B_{rm}	1.4	T	Magnetic remanence of the PMs (Neodymium, type N52)
σ_c	58.58	MS/m	Electrical conductivity of copper wire

Table 2.1. Geometrical and Material Parameters of the AC and PMs in the FE Model Developed in COMSOL Multiphysics Software (COMSOL v.5.4, 2018).

Parameter	Value	Unit	Description
f_b	3.5	Hz	Frequency of the base excitation
$\ddot{u}_{bXmax}$	0.05g	m/s^2	Maximum acceleration of the base excitation ($u_{bXmax}=\ddot{u}_{bXmax}/\omega_b^2$=15.2 cm)
f_s	3.5	Hz	Frequency of the SDOF system
ξ_s	5	%	Critical mechanical damping ratio of the SDOF system
m_s	41.8	gr	Mass of the SDOF system ($m_s=m_w$=41.8 gr)
R_c	129	mΩ	Resistance of the AC
R_l	129	mΩ	Resistance of the electrical load (R_l/R_c=1)
f_b	3.5	Hz	Frequency of the base excitation

Table 2.2. Parameters of the SDOF Model Developed in SIMULINK (MATLAB R2017b, 2017).

The SDOF system is subjected to the base excitation $\ddot{u}_{bX}(t)=\ddot{u}_{bXmax}\sin(\omega_b t)$ along the X-axis with $\ddot{u}_{bXmax}$=0.05g, f_b=3.5 Hz, and $0\le t\le 2T_b$ where $T_b=1/f_b$=0.286 s. Table 2.2 shows parameters of the SDOF model. The motion of this system is described by Equation (2-12a). A numerical solver is used in SIMULINK to solve this equation. Figures 2.6(a) to 2.6(c) show time histories of the displacement of the AC, the induced electric current, and the magnetic force acting on the AC. This force is calculated from the analytical model for given values of u_{sX} and I_{ci} and will be compared to the corresponding results calculated from the FE model.

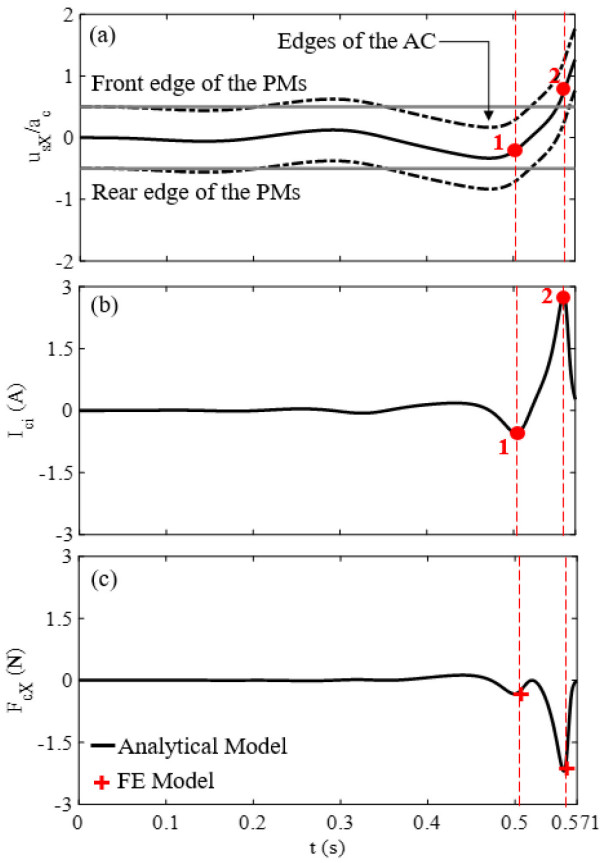

Figure 2.6. Comparison Between the Analytical Model and the FE Model to Calculate the Magnetic Force; (a) Displacement of the AC, (b) Electric Current Induced in the AC, and (c) Magnetic Force F_{cX} Acting on the AC.

Figures 2.6(a) and 2.6(b) show two points 1 and 2 chosen to calculate the magnetic force acting on the AC where u_{sX}=−0.199a_c and +0.733a_c, respectively, for a_c=1 in. These displacements correspond to the electric currents I_{ci}=−0.550 and +2.782 A, respectively. Figure 2.6(c) shows the values of the corresponding magnetic force F_{cX} acting on the AC calculated from the FE model and then compared to the analytical model. There is a good agreement between both the models. This validates the accuracy of the analytical model developed to calculate the magnetic force using Equation (2-5a).

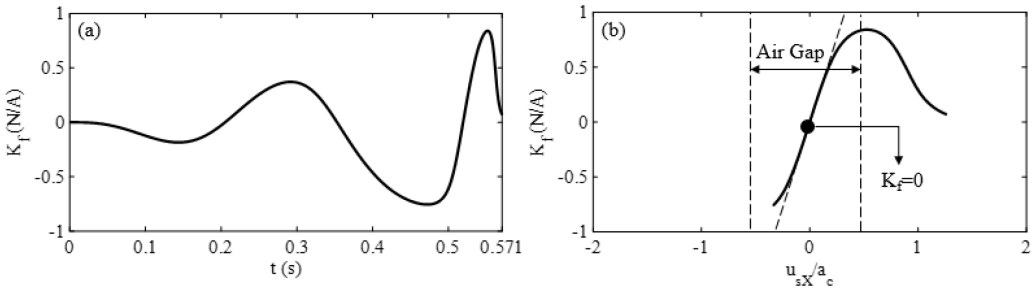

Figure 2.7. Variation of the Electromechanical Coupling Coefficient (EMCC) with (a) Time and (b) Displacement of the AC.

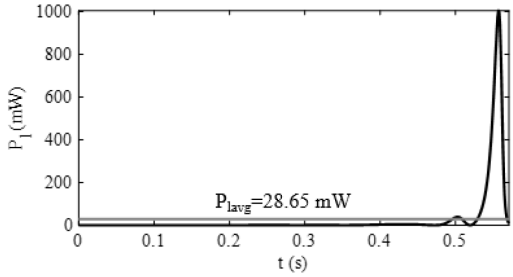

Figure 2.8. Electrical Power Harvested from the Simple EMEH During its First Two Cycles of Vibration.

Figure 2.7(a) shows time history of the EMCC K_f. Figure 2.7(b) also shows variation of this coefficient with the displacement of the AC. It is seen that K_f is maximum at $u_{sX}=\pm 0.5a_c$ and very low at large displacements; approximately beyond two times of the length of the air gap along the X-axis where the mechanical energy domain is decoupled from the electromagnetic energy domain. Figure 2.8 shows time history of instantaneous electrical power harvested from the simple EMEH during its first two cycles of vibration. The peak instantaneous electrical power is 1 W occurred at t=0.557 s. The average electrical power during the first two cycles of vibration is also 28.65 mW.

Subsection 2.5. Results and Discussion

The EMCC K_f is a time-varying parameter in Equation (2-12a). However, a closed-form solution can be achieved for the displacement response of the SDOF system by assuming that this parameter is constant in Equation (2-12a),

$$u_{sX}(t) = \frac{\left(\frac{\omega_b}{\omega_s}\right)^2}{\sqrt{\left[1-\left(\frac{\omega_b}{\omega_s}\right)^2\right]^2+\left[\left(2\xi_s+\frac{K_f^2}{m_s\omega_s(R_l+R_c)}\right)\left(\frac{\omega_b}{\omega_s}\right)\right]^2}} u_{bXmax}\sin(\omega_b t-\phi) \qquad (2\text{-}15a)$$

where ϕ is the phase lag between the base excitation and the response of the SDOF system:

$$\phi = tan^{-1}\left(\left(2\xi_s + \frac{K_f^2}{m_s\omega_s(R_l+R_c)}\right)\frac{\left(\frac{\omega_b}{\omega_s}\right)}{1-\left(\frac{\omega_b}{\omega_s}\right)^2}\right) \qquad (2\text{-}15b)$$

The largest amount of electric power can be delivered by the EMEH under a resonant condition, that is, when the frequency of the SDOF system matches that of the base excitation, i.e. $\omega_b=\omega_s$. The velocity response of the SDOF system under resonant condition is,

$$\dot{u}_{sX}(t) = +\frac{m_s\omega_b^2(R_l+R_c)}{2\xi_s m_s\omega_b(R_l+R_c)+K_f^2}u_{bXmax}\sin(\omega_b t-\phi) \qquad (2\text{-}16)$$

By substituting $\dot{u}_{sX}(t)$ into Equation (2-13), average electric power P_{lavg} can be obtained in term of R_l as follows,

$$P_{lavg} = \frac{1}{2}\frac{K_f^2 m_s^2\omega_b^4 R_l}{\left[2\xi_s m_s\omega_b(R_l+R_c)+K_f^2\right]^2}u_{Xbmax}^2 \qquad (2\text{-}17)$$

The maximum average electric power can be calculated by putting the derivative of P_{lavg} with respect to R_l equal to zero that results in the calculation of the optimal load resistance as follows (Stephen, 2006),

$$R_{lopt} = R_c + \frac{K_f^2}{2\xi_s m_s\omega_b} \qquad (2\text{-}18a)$$

The maximum average electric power can be then expressed as (Stephen, 2006),

$$P_{lavgmax} = \frac{1}{16}\frac{K_f^2 m_s^2\omega_b^4}{\xi_s m_s\omega_b\left(2\xi_s m_s\omega_b R_c+K_f^2\right)}u_{Xbmax}^2 \qquad (2\text{-}18b)$$

This approach to the calculation of the maximum average electric power is not accurate due to the assumption that K_f is constant. Therefore, the maximum average electric power is calculated numerically by solving Equation (2-12) in SIMULINK. For this purpose, the SDOF system is subjected to the base excitation $\ddot{u}_{bX}(t)=\ddot{u}_{bXmax}\sin(\omega_b t)$ along the X-axis for $\ddot{u}_{bXmax}$=0.01g, 0.05g, and 0.10g and f_b=3.5 Hz over the time interval $0\le t\le 2T_b$ where $T_b=1/f_b$=0.286 s. The proposed EMEH is tuned to undergo the resonant condition with the frequency $f_s=f_b$=3.5 Hz. Table 2.3 shows the electromechanical parameters of the proposed EMEH.

Parametric analysis is carried out to find optimal load resistance of the proposed EMEH for three different intensity levels of base excitation. Figures 2.9(a) to 2.9(d) show the variation of the average electric power versus the ratio of the load resistance to that of the coil R_l/R_c for PMs Array 1, 2, 3, and 4.

Parameter	Value	Unit	Description
a_m	0.5	in	Length of the sides of the PMs
δ_{gmX}	1	mm	Size of the gap between the PMs along the X-axis
δ_{gmY}	1	mm	Size of the gap between the PMs along the Y-axis
n_X	5		Number of the PMs along the X-axis
n_Y	5		Number of the PMs along the Y-axis
a_c	2.5	in	Length of the sides of the AC
h_c	0.5	in	Height of the AC (N_z=13)
t_c	0.5	in	Winding depth (N_t=13)
d_w	1	mm	Diameter of the copper wire (18-AWG)
Δ_{gcZ}	1/16	in	Size of the vertical gap between the AC and the PMs
B_{rm}	1.4	T	Magnetic remanence of the PMs
σ_c	58.58	MS/m	Electrical conductivity of copper wire
f_b	3.5	Hz	Frequency of the base excitation
$\ddot{u}_{bXmax}$	Var.	m/s^2	Maximum acceleration of the base excitation
f_s	3.5	Hz	Frequency of the SDOF system (f_s=f_b)
ξ_s	5	%	Critical mechanical damping ratio of the SDOF system
m_s	241.7	gr	Mass of the SDOF system (m_s=m_w)
R_c	746.4	mΩ	Resistance of the AC
R_l	Var.	mΩ	Resistance of the electrical load

Table 2.3. Electromechanical Parameters of the Proposed EMEH.

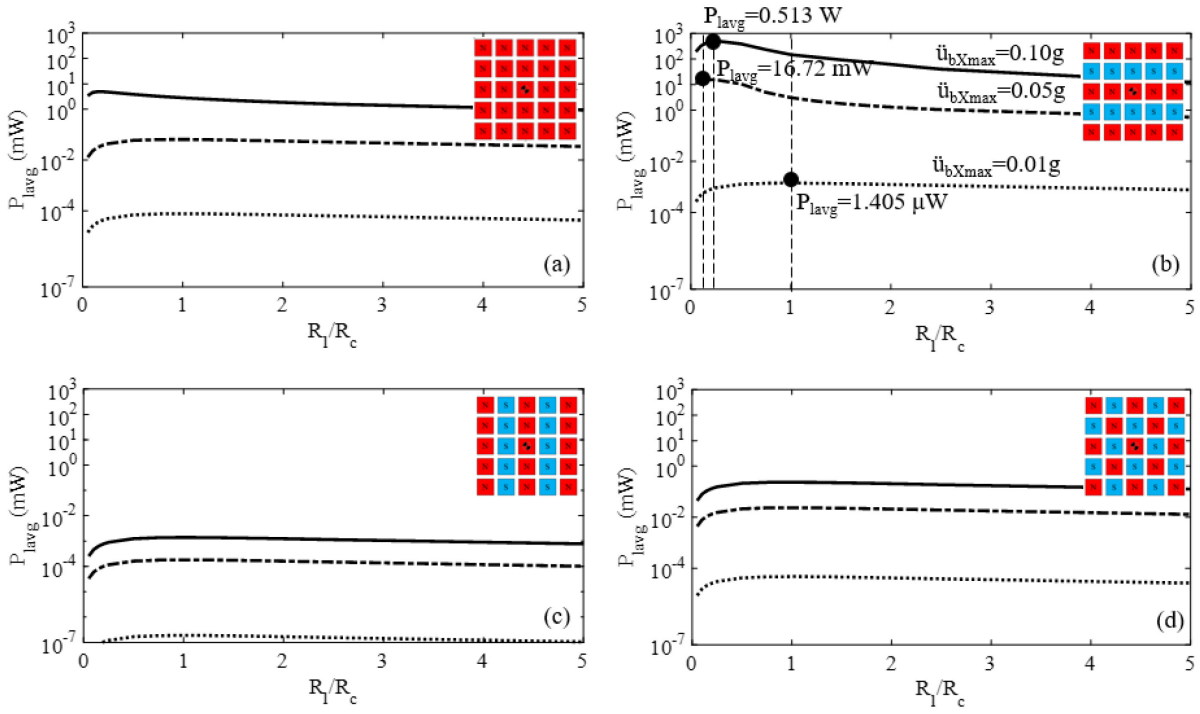

Figure 2.9. Average Electrical Power Harvested from the Proposed EMEH Versus the Ratio of the Load Resistance to the Coil Resistance (R_l/R_c) for (a) PMs Array 1, (b) PMs Array 2, (c) PMs Array 3, and (d) PMs Array 4.

It is seen that the proposed EMEH can deliver the highest electrical power when the PMs are arranged according to array 2 in which the poles alternate along the X-axis. The average electrical power increases with the increase of the intensity of the bases acceleration. It is seen that for $\ddot{u}_{bXmax}$=0.1g the maximum average electric power is equal to $P_{lavgmax}$=513 mW that can be delivered by the load resistance R_l=0.25R_c=186.6 mΩ. The amount of power is relatively very large and can be uses to power conventional sensors used for structural health monitoring of bridges.

Larger electric power can be delivered by adding a greater number of ACs and PMs Arrays installed in parallel. This will be the subject of the next step of the project in which a prototype of the proposed EMEH is fabrication for laboratory and field testing.

Section 3. Design, Fabrication, and Testing of a Proof-of-Concept Prototype

Subsection 3.1. Introduction

This chapter focuses on the design, fabrication, and laboratory and field testing of a proof-of concept prototype of the proposed EMEH. The design of this prototype is based on the model studied in chapter 2.

Subsection 3.2. Design and Fabrication of a Proof-of-Concept Prototype

Figure 3.1 shows the prototype of the proposed EMEH designed and fabricated for the purpose of proof-of-concept testing in both the laboratory and field environments. The configuration of the prototype is based on the design and finite element simulation developed in chapter 2 with slightly difference in the size of the coil. The prototype consists of an aluminum plate of the size 10×10×0.25 in used as the base plate to transfer the base excitation; four springs each one with the stiffness coefficient 191 N/m; an aluminum plate of the size 8×3×0.25 in used to hold a total mass of m_s=1.1 kg on the springs (including the mass of the copper coil and a tip mass of 0.6 kg); a rectangular copper coil with the thickness 0.25 in and the outside size 2.25×2.25 in and the inside size 1.75×1.75 in, two magnetic arrays consisting of 25 cubic neodymium PMs of the size 0.5×0.5×0.5 in with the magnetic remanence of B_{rm}=1.2 T (Neodymium, type N42). The frequency of the system was measured to be approximately about f_s=4 Hz.

It should be noted that, for the sake of fabrication simplicity, the PMs have been arranged according to Array 4 in Figure 2.3. The PMs in this array are in a static force-equilibrium condition that facilitates their arrangement with bare hands. This array causes a lower output voltage compared to Array 2 that has strongest magnetic interaction with the coil as discussed in Figure 2.9. The PMs in each one of the left and right magnetic arrays are arranged in such a way that their opposing poles face the PMs in other array. This strengthens the flow of magnetic flux between the two PMs arrays when passing through the coil as shown in Figure 3.1.

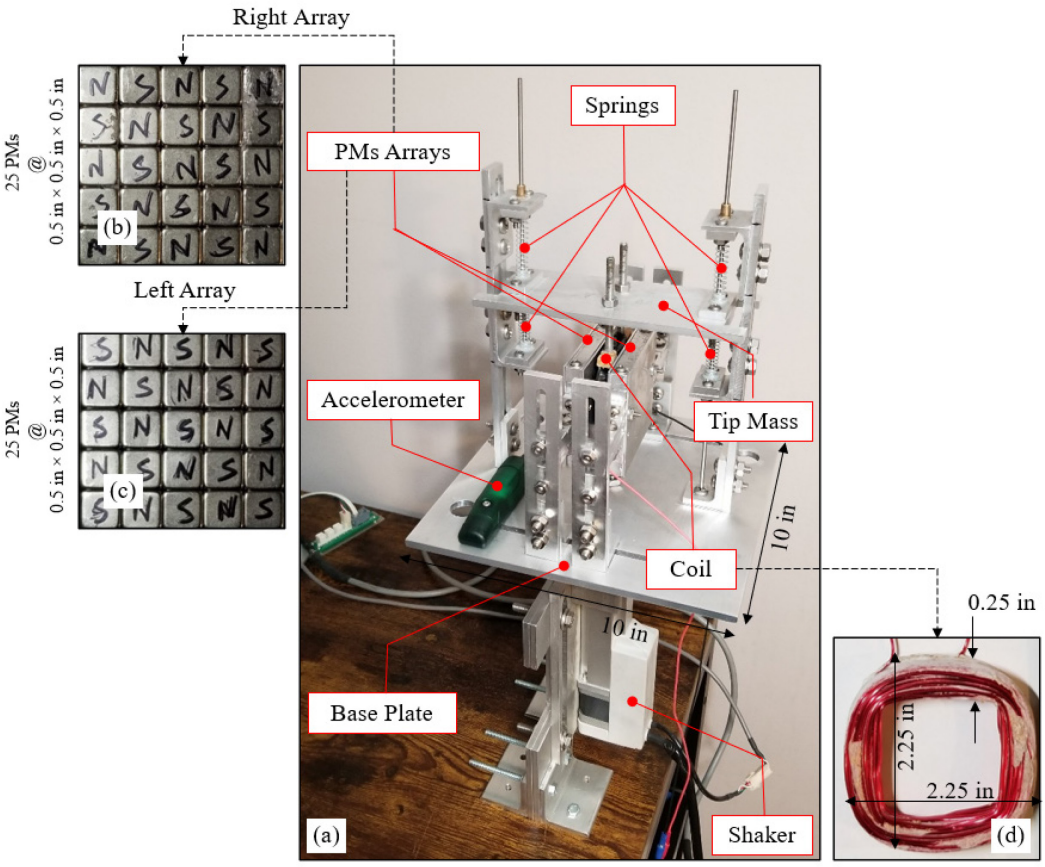

Figure 3.1. Proof-of-concept Prototype of the Proposed EMEH; (a) 3D View of the Fabricated Device in Laboratory with Details on Geometry of (b and c) the PMs Arrays and their Planar Arrangement, and (d) the Copper Coil.

Subsection 3.3. Laboratory Testing

Figure 3.2 shows the lab-bench setup established in a laboratory environment for testing the proof-of-concept prototype of the proposed EMEH under harmonic excitations. The apparatus used in this experiment are a linear servo actuator (Dyadic Systems, SCN5-010-100, AS03) used as a shaker to simulate the harmonic excitation of base, a data logger system (WaveBook 516: Data Acquisition System) to record the output voltage, an acceleration sensor (Accelerometer Data Logger X2-5) to measure the acceleration of the base, and a PC to processes the output signals.

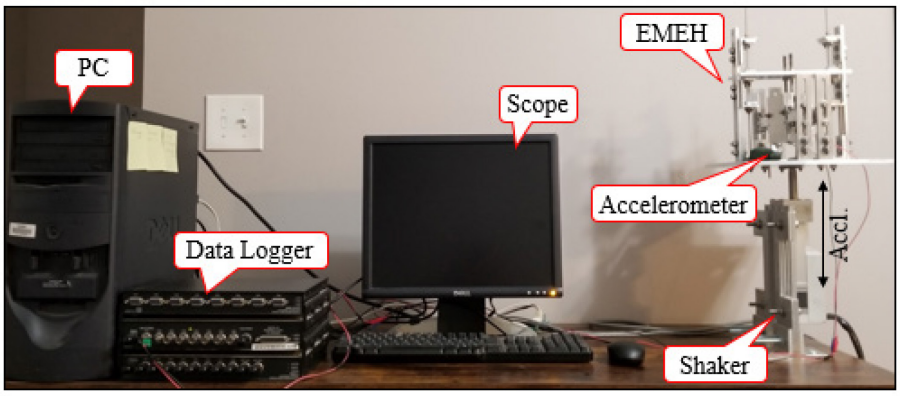

Figure 3.2. Experimental Setup Established to Test the Proof-of-concept Prototype of the Proposed EMEH in a Laboratory Environment under Harmonic Excitations.

The center of the base plate was firmly attached to the shaker to drive the prototype EMEH by programmed harmonic excitations. The data logger was set to measure the time history of voltage at a sampling rate of 1000 Hz. The sensitivity and sampling rate of the accelerometer were set to 64000 LSB/g and 125 Hz, respectively. The maximum acceleration of the harmonic excitation generated by the shaker was set to $\ddot{u}_{bXmax}$=0.2g.

Figure 3.3 shows the power spectral density of the base acceleration for five different motion signals recorded by the accelerometer. These acceleration signals were denoised by a 3rd order band-pass Butterworth filter with the cut-off frequencies 0.5 Hz and 35 Hz and the Nyquist frequency 62.5 Hz defined by the function [b,a]=butter(.) in MATLAB. This figure shows that the range of frequency of the base excitation is from f_b=1.5 Hz to f_b=3.0 Hz. This range is quite short and the frequencies in this range are less than f_s=4 Hz. This was due to the limitation of the actuator in compensating the gravity effects in the vertical direction (i.e. weight of the prototype EMEH). For this reason, exciting the prototype EMEH under a resonant condition when f_b=f_s=4 Hz was not feasible in this experimental study.

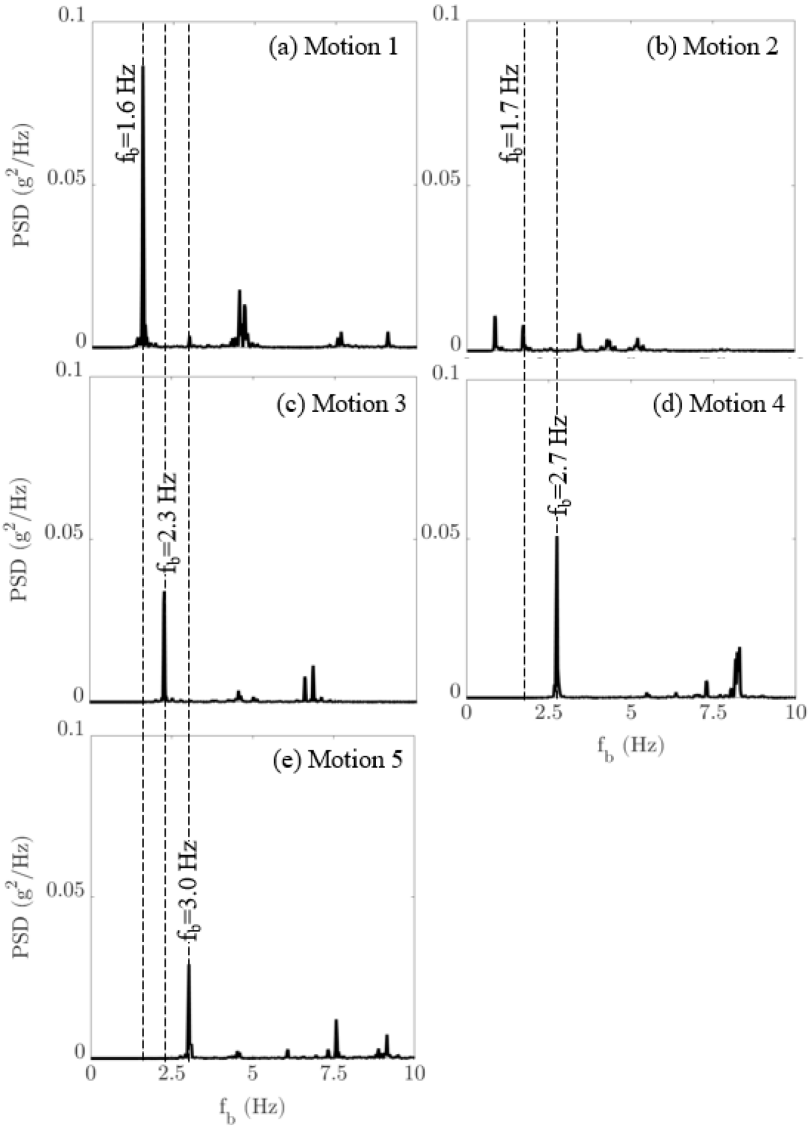

Figure 3.3. Power Spectral Density of the Acceleration of Base Recorded by an Accelerometer of the Model Data Logger X2-5.

Figure 3.4 shows the five voltage signals output from the prototype EMEH when subjected to the five base excitations with PSDs shown in Figure 3.3. These voltage signals were denoised by a 3rd order band-pass Butterworth filter with the cut-off frequencies 3 Hz and 21 Hz and the Nyquist frequency 500 Hz defined by function [b,a]=butter(.) in MATLAB.

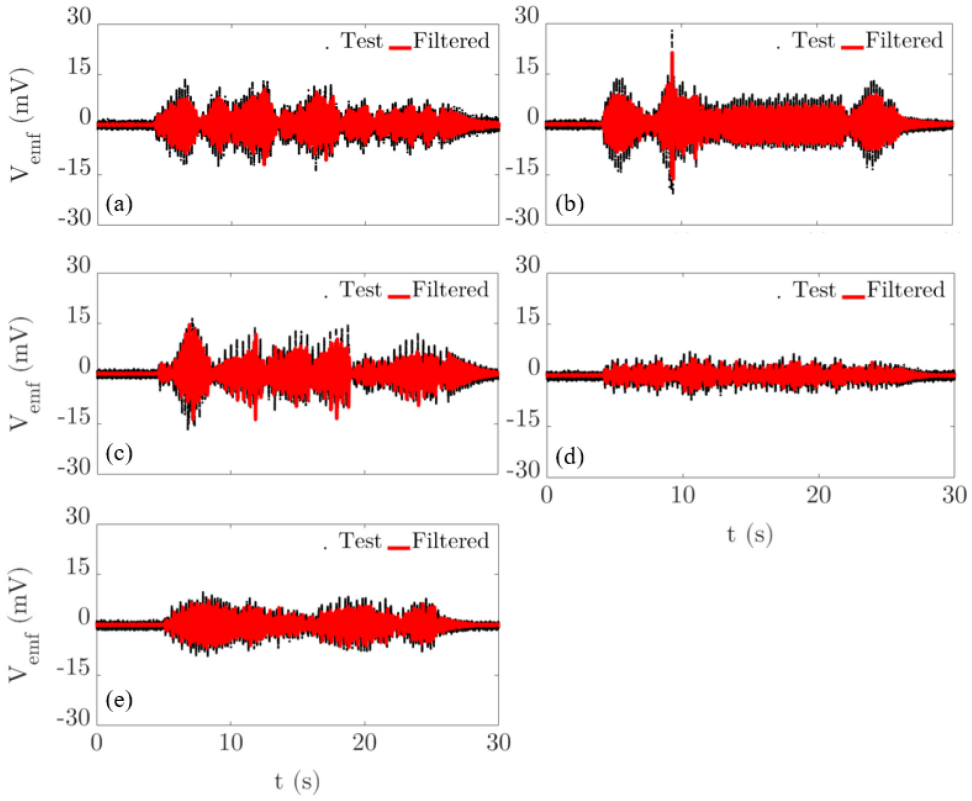

Figure 3.4. Voltage Output from the Prototype EMEH Subjected to Five Different Base Excitations with the Frequencies from f_b=1.5 Hz to f_b=3.0 Hz; RMSs of these Voltage Signals are (a) 2.8 V, (b) 3.9 V, (c) 2.8 V, (d) 1.4 V, and (e) 2.2 V.

The root mean squares (RMSs) of these voltage signals are 2.8 V, 3.9 V, 2.8 V, 1.4 V, and 2.2 V, respectively. It should be noted a much higher voltage can be harvested from the device if one uses the PMs Array 2 in Figure 2.3.

Subsection 3.4. Field Testing

The suspension bridge of the Robert F. Kennedy Bridge (formerly the Tri-borough Bridge) over the East River was selected for the field testing of the proof-of-concept prototype. This bridge connecting Wards Island to Astoria in Queens carries a heavy daily traffic load from Manhattan to Queens (See Figure 3.5(a)). The suspension bridge is subjected to a quite strong vibration induced by this heavy daily traffic.

Figure 3.5. The Robert F. Kennedy Bridge in New York: (a) Geographical Location of the Bridge on the Google Map, and (b) View of the Suspension bridge from Ward's Island with the Testing Location Marked (Photo is taken from the Google Map).

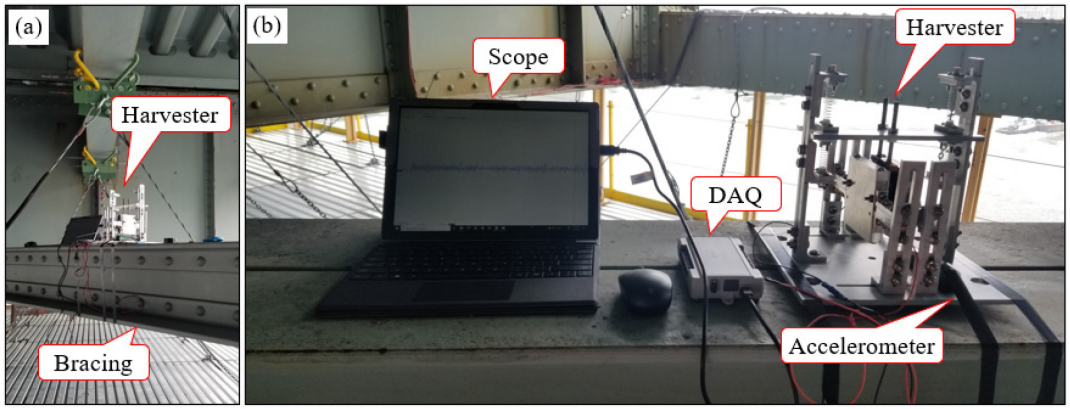

Figure 3.6. Field Testing of the Proof-of-concept Prototype of the Proposed EMEH Installed on the Robert F. Kennedy Bridge in New York: (a) Placement of the Device on the Middle of a Horizontal Lateral Bracing of the Deck, and (b) Testing Setup.

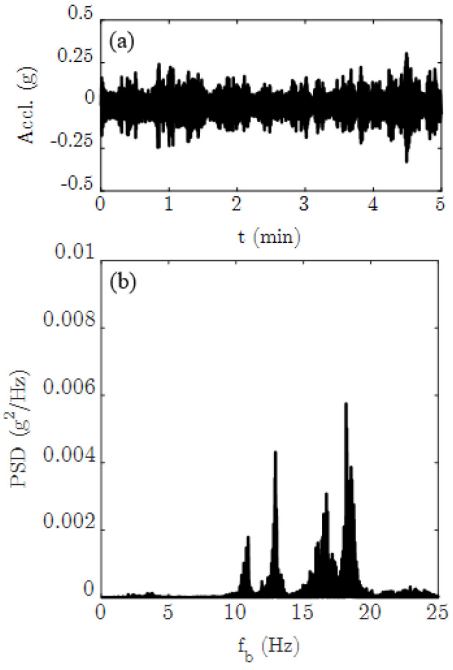

Figure 3.7. Acceleration of the Base Excitation Recorded by an Accelerometer of the Model Data Logger X2-5 During the Field Testing: (a) 5 min Time-history of the Acceleration and (b) Power Spectral Density of the Acceleration.

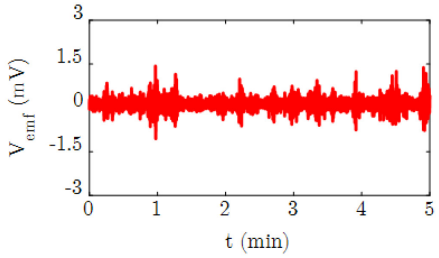

Figure 3.8. Voltage Output from the Prototype EMEH Subjected to Vibration of the Bridge.

The energy harvester was installed on one of the lateral horizontal bracings of the deck of the bridge at a location next to the east tower as shown in Figure 3.5(b). Figure 3.7(a) shows time-history of the acceleration of bridge recorded by an accelerometer of the model Data Logger X2-5 over a time duration of 5 min. Figure 3.7(b) shows the power spectral density of the acceleration signal. It is seen that the bridge has several significant frequencies in a range from f_b=10 Hz to f_b=20 Hz. These frequencies are much larger than the frequency of the prototype which is about f_s=4 Hz. For this reason, it was difficult to put the prototype EMEH into a resonant condition with the vibration of the bridge. Figure 3.8 shows time history of the voltage output from the prototype EMEH during the field test. It is seen that the magnitude of this voltage is less than 1.5 mV.

Section 4. Conclusions

This project focuses on the development of an electromagnetic energy harvester with planar arrays of permanent magnets for harvesting electric power from highway bridges subjected to traffic-induced vibration. The following are the conclusions of this work:

1) A new type of electromagnetic energy harvester has been proposed in which planar arrays of permanent magnets have been employed as the magnetic field source to interact with the moving copper coil. Four different arrangements of the permanent magnets were investigated in the design of this harvester.
2) An electromechanical model was developed to model the magnetic interaction between the magnetic arrays and the copper coil. The accuracy of this analytical model was verified using finite element simulations in COMSOL.
3) The analytical model was used to carry out a parametric analysis on the arrangements of permanent magnets and the electrical resistance of the harvesting circuit under resonance condition. It was found that the proposed EMEH can deliver the highest electrical power when the poles of permanent magnets alternate along the direction of motion. The numerical results showed that for $\ddot{u}_{bXmax}$=0.1g the maximum average electric power is equal to 513 mW that can be delivered by a harvesting circuit with an electrical resistance of 186.6 mΩ.
4) A proof-of-concept prototype of the proposed EMEH was designed and fabricated for the laboratory and field testing.

References

Aladwani, A., Aldraihem, O., Baz, A., 2014. A distributed parameter cantilevered piezoelectric energy harvester with a dynamic magnifier. Mech. Adv. Mater. Struct. 21, 566–578. https://doi.org/10.1080/15376494.2012.699600

Aladwani, A., Arafa, M., Aldraihem, O., Baz, A., 2012. Cantilevered piezoelectric energy harvester with a dynamic magnifier. J. Vib. Acoust. Trans. ASME 134. https://doi.org/10.1115/1.4005824

Aldraihem, O., Baz, A., 2011. Energy Harvester with a Dynamic Magnifier. J. Intell. Mater. Syst. Struct. 22, 521–530. https://doi.org/10.1177/1045389X11402706

Amjadian, M., Agrawal, A.K., 2020. Planar Arrangement of Permanent Magnets in Design of a Magneto-Solid Damper by Finite Element Method. J. Intell. Mater. Syst. Struct.

Amjadian, M., Agrawal, A.K., 2019. Feasibility study of using a semiactive electromagnetic friction damper for seismic response control of horizontally curved bridges. Struct. Control Heal. Monit. e2333. https://doi.org/10.1002/stc.2333

Amjadian, M., Agrawal, A.K., 2018. Modeling, design, and testing of a proof-of-concept prototype damper with friction and eddy current damping effects. J. Sound Vib. 413, 225–249. https://doi.org/10.1016/j.jsv.2017.10.025

Amjadian, M., Agrawal, A.K., 2017. A passive electromagnetic eddy current friction damper (PEMECFD): Theoretical and analytical modeling. Struct. Control Heal. Monit. 24, e1978. https://doi.org/10.1002/stc.1978

Asadi, E., Askari, H., Behrad Khamesee, M., Khajepour, A., 2017. High frequency nano electromagnetic self-powered sensor: Concept, modelling and analysis. Meas. J. Int. Meas. Confed. 107, 31–40. https://doi.org/10.1016/j.measurement.2017.04.019

Beeby, S.P., Torah, R.N., Tudor, M.J., Glynne-Jones, P., O'Donnell, T., Saha, C.R., Roy, S., 2007. A micro electromagnetic generator for vibration energy harvesting. J. Micromechanics Microengineering 17, 1257–1265. https://doi.org/10.1088/0960-1317/17/7/007

Biswas, S.P., Roy, P., Patra, N., Mukherjee, A., Dey, N., 2016. Intelligent traffic monitoring system. Adv. Intell. Syst. Comput. 380, 535–545. https://doi.org/10.1007/978-81-322-2523-2_52

Cannarella, J., Selvaggi, J., Salon, S., Tichy, J., Borca-Tasciuc, D.A., 2011. Coupling factor between the magnetic and mechanical energy domains in electromagnetic power harvesting applications. IEEE Trans. Magn. 47, 2076–2080. https://doi.org/10.1109/TMAG.2011.2122265

Chen, S.N., Wang, G.J., Chien, M.C., 2006. Analytical modeling of piezoelectric vibration-induced micro power generator. Mechatronics 16, 379–387. https://doi.org/10.1016/j.mechatronics.2006.03.003

Cho, S., Jang, S.A., Jo, H., Mechitov, K., Rice, J.A., Jung, H.-J., Yun, C.-B., Spencer, Jr., B.F., Nagayama, T., Seo, J., 2010. Structural health monitoring system of a cable-stayed bridge using a dense array of scalable smart sensor network, in: Tomizuka, M. (Ed.), Sensors and Smart Structures Technologies for Civil, Mechanical, and Aerospace Systems 2010. SPIE, p. 764707. https://doi.org/10.1117/12.852272

COMSOL v.5.4, 2018. Multiphysics® Modeling Software v.5.4.

DuToit, N.E., Wardle, B.L., Kim, S.G., 2005. Design considerations for MEMS-scale piezoelectric mechanical vibration energy harvesters, in: Integrated Ferroelectrics. Taylor & Francis Group , pp. 121–160. https://doi.org/10.1080/10584580590964574

El-hami, M., Glynne-Jones, P., White, N.M., Hill, M., Beeby, S., James, E., Brown, A.D., Ross, J.N., 2001. Design and fabrication of a new vibration-based electromechanical power generator. Sensors Actuators, A Phys. 92, 335–342. https://doi.org/10.1016/S0924-4247(01)00569-6

Elvin, N.G., Elvin, A.A., 2011. An experimentally validated electromagnetic energy harvester, in: Journal of Sound and Vibration. Academic Press, pp. 2314–2324. https://doi.org/10.1016/j.jsv.2010.11.024

Erturk, A., Inman, D.J., 2008. A distributed parameter electromechanical model for cantilevered piezoelectric energy harvesters. J. Vib. Acoust. Trans. ASME 130. https://doi.org/10.1115/1.2890402

Foisal, A.R.M., Hong, C., Chung, G.S., 2012. Multi-frequency electromagnetic energy harvester using a magnetic spring cantilever. Sensors Actuators, A Phys. 182, 106–113. https://doi.org/10.1016/j.sna.2012.05.009

Fu, Y., Ouyang, H., Davis, R.B., 2019. Triboelectric energy harvesting from the vibro-impact of three cantilevered beams. Mech. Syst. Signal Process. 121, 509–531. https://doi.org/10.1016/j.ymssp.2018.11.043

Furlani, E.P., 2001. Permanent magnet and electromechanical devices, Foundations. Academic Press. https://doi.org/10.1016/B978-012269951-1/50005-X

Halim, M.A., Cho, H., Park, J.Y., 2015. Design and experiment of a human-limb driven, frequency up-converted electromagnetic energy harvester. Energy Convers. Manag. 106, 393–404. https://doi.org/10.1016/j.enconman.2015.09.065

Halim, M.A., Park, J.Y., 2015. Piezoceramic based wideband energy harvester using impact-enhanced dynamic magnifier for low frequency vibration, in: Ceramics International. Elsevier Ltd, pp. S702–S707. https://doi.org/10.1016/j.ceramint.2015.03.143

Halim, M.A., Park, J.Y., 2014. Performance enhancement of a low frequency vibration driven 2-DOF piezoelectric energy harvester by mechanical impact [WWW Document]. J. Phys. Conf. Ser. https://doi.org/10.1088/1742-6596/557/1/012093

Haodong, L., Pillay, P., 2007. A linear generator powered from bridge vibrations for wireless sensors, in: Conference Record - IAS Annual Meeting (IEEE Industry Applications Society). pp. 523–529. https://doi.org/10.1109/07ias.2007.85

Jung, H.-J., Kim, I.-H., Jang, S.-J., 2011. An energy harvesting system using the wind-induced vibration of a stay cable for powering a wireless sensor node. Smart Mater. Struct. 20, 075001. https://doi.org/10.1088/0964-1726/20/7/075001

Khaligh, A., Zeng, P., Zheng, C., 2010. Kinetic energy harvesting using piezoelectric and electromagnetic technologiesstate of the art. IEEE Trans. Ind. Electron. 57, 850–860. https://doi.org/10.1109/TIE.2009.2024652

Kong, N., Ha, D.S., Erturk, A., Inman, D.J., 2010. Resistive Impedance Matching Circuit for Piezoelectric Energy Harvesting. J. Intell. Mater. Syst. Struct. 21, 1293–1302. https://doi.org/10.1177/1045389X09357971

Kwon, S.-D., Park, J., Law, K., 2013. Electromagnetic energy harvester with repulsively stacked multilayer magnets for low frequency vibrations. Smart Mater. Struct. 22, 055007. https://doi.org/10.1088/0964-1726/22/5/055007

Li, K., He, X., Wang, X., Jiang, S., 2019. A Nonlinear Electromagnetic Energy Harvesting System for Self-Powered Wireless Sensor Nodes. J. Sens. Actuator Networks 8, 18. https://doi.org/10.3390/jsan8010018

Li, X., Upadrashta, D., Yu, K., Yang, Y., 2019. Analytical modeling and validation of multi-mode piezoelectric energy harvester. Mech. Syst. Signal Process. 124, 613–631. https://doi.org/10.1016/j.ymssp.2019.02.003

Liang, J., Liao, W.-H., 2010. Impedance matching for improving piezoelectric energy harvesting systems, in: Ghasemi-Nejhad, M.N. (Ed.), Active and Passive Smart Structures and Integrated Systems 2010. SPIE, p. 76430K. https://doi.org/10.1117/12.847524

Liu, X., Qiu, J., Chen, H., Xu, X., Wen, Y., Li, P., 2015. Design and Optimization of an Electromagnetic Vibration Energy Harvester Using Dual Halbach Arrays. IEEE Trans. Magn. 51. https://doi.org/10.1109/TMAG.2015.2437892

MATLAB R2017b, 2017. MATLAB (R2017b). MathWorks Inc. https://doi.org/10.1007/s10766-008-0082-5

Mikoshiba, K., Manimala, J.M., Sun, C., 2013. Energy harvesting using an array of multifunctional resonators. J. Intell. Mater. Syst. Struct. 24, 168–179. https://doi.org/10.1177/1045389X12460335

Mösch, M., Fischerauer, G., 2019. A Comparison of Methods to Measure the Coupling Coefficient of Electromagnetic Vibration Energy Harvesters. Micromachines 10, 826. https://doi.org/10.3390/mi10120826

Nedelchev, K., Kralov, I., 2017. Efficiency improvement of a vibration energy harvesting generator by using additional vibrating system, in: AIP Conference Proceedings. American Institute of Physics Inc., p. 020015. https://doi.org/10.1063/1.5013952

Paul, C.R., 2009. Inductance, Inductance: Loop and Partial. John Wiley & Sons, Inc., Hoboken, NJ, USA. https://doi.org/10.1002/9780470561232

Peigney, M., Siegert, D., 2020. Low-Frequency Electromagnetic Energy Harvesting from Highway Bridge Vibrations. J. Bridg. Eng. 25, 04020056. https://doi.org/10.1061/(ASCE)BE.1943-5592.0001581

Priya, S., 2007. Advances in energy harvesting using low profile piezoelectric transducers. J. Electroceramics 19, 165–182. https://doi.org/10.1007/s10832-007-9043-4

Priya, S., Inman, D.J., 2009. Energy harvesting technologies, Energy Harvesting Technologies. Springer US. https://doi.org/10.1007/978-0-387-76464-1

Robertson, W., Cazzolato, B., Zander, A., 2012. Axial force between a thick coil and a cylindrical permanent magnet: Optimizing the geometry of an electromagnetic actuator. IEEE Trans. Magn. 48, 2479–2487. https://doi.org/10.1109/TMAG.2012.2194789

Salauddin, M., Halim, M.A., Park, J.Y., 2016. A magnetic-spring-based, low-frequency-vibration energy harvester comprising a dual Halbach array. Smart Mater. Struct. 25, 095017. https://doi.org/10.1088/0964-1726/25/9/095017

Sams, H.W., 1986. Handbook of electronics tables and formulas. Howard W. Sams & Co.

Sazonov, E., Pillay, P., Li, H., Curry, D., 2009. Self-Powered Sensors for Monitoring of Highway Bridges. IEEE Sens. J. 9, 1422–1429. https://doi.org/10.1109/JSEN.2009.2019333

Shen, W., Zhu, S., Xu, Y.-L., Zhu, H., 2018. Energy regenerative tuned mass dampers in high-rise buildings. Struct. Control Heal. Monit. 25, e2072. https://doi.org/10.1002/stc.2072

Singhal, A., Kamga, C., Agrawal, A.K., 2018. LADAR-based collision warning sensor to prevent over-height vehicle bridge hits. IET Intell. Transp. Syst. 12, 689–695. https://doi.org/10.1049/iet-its.2017.0117

Sodano, H.A., Park, G., Inman, D.J., 2004. Estimation of electric charge output for piezoelectric energy harvesting. Strain 40, 49–58. https://doi.org/10.1111/j.1475-1305.2004.00120.x

Soliman, M.S.M., Abdel-Rahman, E.M., El-Saadany, E.F., Mansour, R.R., 2008. A wideband vibration-based energy harvester. J. Micromechanics Microengineering 18. https://doi.org/10.1088/0960-1317/18/11/115021

Spencer, B.F., Jo, H., Mechitov, K.A., Li, J., Sim, S.H., Kim, R.E., Cho, S., Linderman, L.E., Moinzadeh, P., Giles, R.K., Agha, G., 2016. Recent advances in wireless smart sensors for multi-scale monitoring and control of civil infrastructure. J. Civ. Struct. Heal. Monit. 6, 17–41. https://doi.org/10.1007/s13349-015-0111-1

Stephen, N.G., 2006. On energy harvesting from ambient vibration. J. Sound Vib. 293, 409–425. https://doi.org/10.1016/j.jsv.2005.10.003

Tadesse, Y., Shujun Zhang, Priya, S., 2009. Multimodal Energy Harvesting System: Piezoelectric and Electromagnetic. J. Intell. Mater. Syst. Struct. 20, 625–632. https://doi.org/10.1177/1045389X08099965

Wang, H. yan, Tang, L. hua, Guo, Y., Shan, X. biao, Xie, T., 2014. A 2DOF hybrid energy harvester based on combined piezoelectric and electromagnetic conversion mechanisms. J. Zhejiang Univ. Sci. A 15, 711–722. https://doi.org/10.1631/jzus.A1400124

Wei, C., Jing, X., 2017. A comprehensive review on vibration energy harvesting: Modelling and realization. Renew. Sustain. Energy Rev. https://doi.org/10.1016/j.rser.2017.01.073

Williams, C.B., Yates, R.B., 1996. Analysis of a micro-electric generator for microsystems. Sensors Actuators, A Phys. 52, 8–11. https://doi.org/10.1016/0924-4247(96)80118-X

Xu, Z., Shan, X., Chen, D., Xie, T., 2016. A Novel Tunable Multi-Frequency Hybrid Vibration Energy Harvester Using Piezoelectric and Electromagnetic Conversion Mechanisms. Appl. Sci. 6, 10. https://doi.org/10.3390/app6010010

Yang, B., Lee, C., Xiang, W., Xie, J., Han He, J., Kotlanka, R.K., Low, S.P., Feng, H., 2009. Electromagnetic energy harvesting from vibrations of multiple frequencies. J. Micromechanics Microengineering 19. https://doi.org/10.1088/0960-1317/19/3/035001

Zeng, P., Khaligh, A., 2013. A permanent-magnet linear motion driven kinetic energy harvester. IEEE Trans. Ind. Electron. 60, 5737–5746. https://doi.org/10.1109/TIE.2012.2229674

Zhou, W., Penamalli, G.R., Zuo, L., 2012. An efficient vibration energy harvester with a multi-mode dynamic magnifier. Smart Mater. Struct. 21, 015014. https://doi.org/10.1088/0964-1726/21/1/015014

Zhu, S., Shen, W. ai, Xu, Y. lin, 2012. Linear electromagnetic devices for vibration damping and energy harvesting: Modeling and testing. Eng. Struct. 34, 198–212. https://doi.org/10.1016/j.engstruct.2011.09.024

Zuo, L., Cui, W., 2013. Dual-functional energy-harvesting and vibration control: Electromagnetic resonant shunt series tuned mass dampers. J. Vib. Acoust. Trans. ASME 135. https://doi.org/10.1115/1.4024095